

1 **Low-temperature thermochronology of the Indus Basin in central Ladakh, northwest India:**  
2 **Implications of Miocene–Pliocene cooling in the India-Asia collision zone**

3 Gourab Bhattacharya<sup>1,2\*</sup>, Delores M. Robinson<sup>1,2</sup>, Devon A. Orme<sup>3</sup>, Yani Najman<sup>4</sup>, Andrew  
4 Carter<sup>5</sup>

5 <sup>1</sup>*Department of Geological Sciences, The University of Alabama, AL-35487, USA*

6 <sup>2</sup>*Center for Sedimentary Basin Studies, The University of Alabama, AL-35487, USA*

7 <sup>3</sup>*Department of Earth Sciences, Montana State University, MT-59717, USA*

8 <sup>4</sup>*Lancaster Environment Centre, Lancaster University, LA-14YQ, UK*

9 <sup>5</sup>*Department of Earth & Planetary Sciences, Birkbeck, University of London, WC1E 7HX, UK*

10 *\*Corresponding author: gbhattacharya1@crimson.ua.edu*

11

12 **Abstract:** The India-Asia collision zone in Ladakh, northwest India, records a sequence of  
13 tectono-thermal events in the interior of the Himalayan orogen following the intercontinental  
14 collision between India and Asia in early Cenozoic time. We present zircon fission-track, and  
15 zircon and apatite (U-Th)/He thermochronometric data from the Indus Basin sedimentary rocks  
16 that are exposed along the strike of the collision zone in central Ladakh. These data reveal a post-  
17 depositional Miocene–Pliocene (~22–4 Ma) cooling signal along the India-Asia collision zone in  
18 northwest India. Our ZFT cooling ages indicate that maximum basin temperatures exceeded 200  
19 °C but stayed below 280–300 °C in the stratigraphically deeper marine and continental strata.  
20 Thermal modeling of zircon and apatite (U-Th)/He cooling ages suggests post-depositional basin  
21 cooling initiated in Early Miocene time by ~22–20 Ma, occurred throughout the basin across zircon

22 (U-Th)/He partial retention temperatures from ~20–10 Ma, and continued in the Pliocene time  
23 until at least ~4 Ma. We attribute the burial of the Indus Basin to sedimentation and movement  
24 along the regional Great Counter thrust. The ensuing Miocene–Pliocene cooling resulted from  
25 erosion by the Indus River that transects the basin. An approximately coeval cooling signal is well  
26 documented east of the study area, along the collision zone in south Tibet. Our new data provide  
27 a regional framework upon which future studies can explore the possible interrelationships  
28 between tectonic, geodynamic and geomorphologic factors contributing to Miocene–Pliocene  
29 cooling along the India-Asia collision zone from NW India to south Tibet.

30

31 Keywords: Indus Basin, exhumation, cooling, thermochronology, India-Asia collision zone,  
32 Ladakh

## 33 1. Introduction

34 The India-Asia collision zone developed when the Neo-Tethyan ocean closed following  
35 the continent-continent collision between India and Asia in early Cenozoic time (e.g., Searle, 2019;  
36 Kapp and DeCelles, 2019). The sedimentary basins along the collision zone present a natural  
37 laboratory to test models of deposition and exhumation in the interior of the Himalayan orogenic  
38 system. The collision zone in Ladakh, northwest (NW) India exposes the Indus Molasse or the  
39 Indus Basin sedimentary rocks (IBSR), which are a linear suite of deformed marine and continental  
40 strata that were discontinuously deposited from Late Cretaceous to Pliocene time (Figures 1A–B;  
41 Garzanti and Van Haver, 1988; Searle et al., 1990; Clift et al., 2002; Henderson et al., 2010; 2011).  
42 Thus, the IBSR present an opportunity to study the pre- and syn-collisional tectono-thermal events  
43 associated with the evolution of the intercontinental suture zone between India and Asia. Knowing  
44 the timing and extent of suture zone basin exhumation is critical to understanding the surficial-to-  
45 lithospheric scale processes triggering it, which are intrinsically linked to the geological evolution  
46 of the orogenic hinterland.

47 Previous studies on the thermal history of the IBSR along the collision zone in NW India  
48 and on coeval rocks along the collision zone in south Tibet yield different exhumation histories.  
49 Carrapa et al. (2014) present (U-Th)/He detrital zircon (ZHe) and apatite fission-track (AFT)  
50 cooling ages from the Late Oligocene–Early Miocene Kailas Formation of the Yarlung suture in  
51 south Tibet, which record basin exhumation from ~21–15 Ma. The authors interpret that these  
52 cooling ages reflect incision by the paleo-Yarlung River as the Indian plate underthrusts beneath  
53 Asia. In addition, Tremblay et al. (2015) and Orme (2019) document Early–Middle Miocene (~21–  
54 11 Ma) cooling in the Gangdese batholith and the Xigaze forearc basin in south Tibet, thereby  
55 emphasizing that Miocene cooling along the India-Asia collision zone was a regional thermal

56 event. By contrast, in NW India, Tripathy-Lang et al. (2013) report ~52–28 Ma ZHe cooling ages  
57 from the Kailas-contemporaneous Late Oligocene Basgo Formation. Unlike post-depositional  
58 Miocene cooling as recorded in south Tibet, the ZHe cooling ages of the Basgo Formation in NW  
59 India are interpreted to be unreset after deposition and are attributed to exhumation of the source  
60 – the rapidly-eroding Indian margin (Tripathy-Lang et al., 2013). The only previously reported  
61 evidence of post-depositional Miocene cooling in the IBSR is limited to two AFT ages of ~14–12  
62 Ma (Clift et al., 2002) and a single AFT age of ~7 Ma (Schlup et al., 2003). However, ZFT, ZHe  
63 and AFT ages from the Ladakh batholith to the north of the IBSR indicate rapid cooling along the  
64 collision zone in NW India at ~26–18 Ma (Kirstein et al., 2006).

65 To determine if a Miocene cooling signal is present across different formations in the Indus  
66 Basin in NW India, we sampled the IBSR across 4 traverses in central Ladakh: Temesgam and  
67 Basgo sections in the west, Zaskar Gorge in the center, and Upshi-Lato section in the east (Figure  
68 1A). We present ZFT, ZHe and (U-Th)/He detrital apatite (AHe) data to resolve the thermal history  
69 of the IBSR and investigate the underlying causes that contributed to the heating and cooling along  
70 the India-Asia collision zone in NW India.

## 71 **2. Geologic Background**

### 72 **2.1 Tectonic Setting**

73 From south to north, the India-Asia collision zone in NW India (Figures 1B–C) is  
74 composed of: a) the Precambrian–Paleocene Greater Indian passive margin metasedimentary and  
75 sedimentary rocks of the Tethyan Himalaya with an isolated klippe of the Cretaceous Spongtang  
76 oceanic arc (Garzanti et al., 1987; Buckman et al., 2018), b) the Indus Suture Zone containing the  
77 Lamayuru Complex – the Mesozoic deep-water slope facies of the Indian margin (Robertson and

78 Sharp, 1998), and the Dras-Nidar Complexes – an assemblage of Cretaceous ophiolitic mélange,  
79 volcanic and volcano-sedimentary units (Ahmad et al., 2008; Walsh et al., 2019; Das et al., 2020),  
80 c) the Late Cretaceous-Pliocene IBSR (Garzanti and Van Haver, 1988; Searle et al., 1990), and d)  
81 the southern edge of the Early Cretaceous–Early Eocene Ladakh batholith (Weinberg and Dunlap,  
82 2000). The IBSR unconformably overlies the Ladakh batholith to the north and are in fault contact  
83 with the Dras-Nidar Complexes to the south (Figures 1A, C; Searle et al., 1990; St-Onge et al.,  
84 2010). Pre-collisional deposition of the IBSR initiated in an arc-bounded or forearc marine basin  
85 in Late Cretaceous time, and the depocenter evolved into a continental intermontane basin with  
86 the onset of India-Asia collision in Early Eocene time (Garzanti and van Haver, 1988; Henderson  
87 et al., 2010). Regional IBSR deposition largely ended by Late Oligocene–Early Miocene time  
88 (~26–23 Ma) when basin inversion began, although local-scale deposition continued in Pliocene  
89 time in patches of western and central Ladakh (Mathur, 1983; Clift et al., 2002, Henderson et al.,  
90 2010, 2011; Zhou et al., 2020; Bhattacharya et al., 2020).

91 Structurally, the IBSR constitutes the footwall of the regional north-vergent Main Zaskar  
92 backthrust (Searle et al., 1997), also known as the Great Counter thrust (GCT, Figure 1A). Multiple  
93 strike-parallel, north-vergent thrusts belonging to the GCT system deform the IBSR (Steck, 2003).  
94 The timing of movement along the GCT in NW India is indirectly constrained to 23–20 Ma on the  
95 basis of the age of tectonic and metamorphic processes in the Himalayan orogen. Using  $^{40}\text{Ar}/^{39}\text{Ar}$   
96 hornblende ages, Searle et al. (1992) determine that peak metamorphism (700–750 °C, 8 kbar) and  
97 maximum crustal thickening in the Zaskar Himalaya (Figure 1A) south of the GCT occurred at  
98 ~28–23 Ma. Sinclair and Jaffey (2001) and Clift et al. (2002) suggest that this episode of crustal  
99 thickening and uplift in the Himalayan wedge at ~28–23 Ma provided the mechanical force to  
100 initiate movement along the GCT at ~23–20 Ma, thereby inverting the IBSR. Recent studies from

101 south Tibet, based on geochronology-thermochronology datasets and cross-cutting relationships  
102 among Neogene intrusive rocks, also indicate that motion along the GCT initiated at ~23 Ma and  
103 largely ended by ~15 Ma (Zhang et al., 2011; Carrapa et al., 2014; Laskowski et al., 2018; Orme,  
104 2019).

## 105 2.2 Stratigraphy

106 The IBSR stratigraphy comprises two major rock groups (Table 1, Figures 1C, 2A-C): (a)  
107 the southern Late Cretaceous–Early Eocene marine Tar Group (Figures 2B-C), and (b) the northern  
108 Early Eocene to Pliocene continental Indus Group (Figure 2A-C). The Tar Group consists of  
109 carbonate and siliciclastic rocks that are tectonically bounded to the south by the pre-collisional  
110 Dras-Lamayuru-Nidar Complexes and are juxtaposed in the north against the Indus Group. The  
111 Indus Group exhibits extreme along-strike variations in siliciclastic fluvial facies that  
112 unconformably overlie the Ladakh batholith (Brookfield and Andrews-Speed, 1984; Garzanti and  
113 Van Haver, 1988; Searle et al., 1990; Sinclair and Jaffrey, 2001; Clift et al., 2002; Steck, 2003;  
114 Wu et al., 2007; St-Onge et al., 2010; Henderson et al., 2010, 2011; Tripathy-Lang et al., 2013;  
115 Singh et al., 2015; Zhou et al., 2020; Bhattacharya et al., 2020). The Indus Group is categorized  
116 into two sub-groups: (i) the Early Eocene–Early Miocene Lower Indus Group and (ii) the Pliocene  
117 Upper Indus Group. The former is regionally present along the India-Asia collision zone, while  
118 the latter is localized to central and far-western Ladakh (Mathur, 1983; Henderson, et al., 2010).

## 119 2.3 Previous Low-temperature Thermochronometric Studies

120 Low-temperature thermochronologic data and other thermal proxies from the IBSR are  
121 limited to a few local studies with conflicting interpretations, leaving the regional thermal history  
122 undetermined. K/Ar mica ages from phyllites of the Indus Basin indicate a low-grade anchizonal

123 metamorphic event along its southwestern margin in Middle–Late Eocene time, when fold-thrust  
124 deformation occurred in the Tethyan Himalaya (Van Haver et al., 1986; Steck, 2003). Using illite  
125 crystallinity and vitrinite reflectance, Van Haver (1984) determined peak basin temperatures of  
126 ~280 °C in the uppermost Tar Group (Nummulitic Limestone Formation, Figure 2B) and ~155 °C  
127 in the Lower Indus Group. Clift et al. (2002) report 14–12 Ma AFT ages from two Lower Indus  
128 Group samples and interpret that these ages reflect cooling following basin inversion associated  
129 with regional counterthrusting along the GCT at ~23–20 Ma. Illite crystallinity estimates by Clift  
130 et al. (2002) in central Ladakh suggests temperatures did not exceed 200 °C in the Indus Group.  
131 Another paleo-geotemperature study from the Indus Group in eastern Ladakh by Schlup et al.  
132 (2003), which is also discussed in Clift et al. (2004), reveals an illite crystallinity index of 0.36  
133 ( $^{\circ}\Delta 2\theta$ ) from a single Lower Indus Group sandstone sample. This illite crystallinity value translates  
134 to a lower anchizone grade burial temperature of ~239°C using the index-temperature equation of  
135 Zhu et al. (2016). Schlup et al. (2003) also report a ZFT central age of  $23 \pm 2$  Ma and an AFT age  
136 of  $7.4 \pm 0.7$  Ma from the same sandstone sample. The  $23 \pm 2$  Ma ZFT age is interpreted to reflect  
137 source cooling and is attributed to the exhumation of the Ladakh batholith, while the  $7.4 \pm 0.7$  Ma  
138 AFT age suggests post-depositional cooling in the basin. Tripathy-Lang et al. (2013) report unreset  
139 ZHe ages of ~52–28 Ma in the Lower Indus Group Late Oligocene Basgo Formation and attribute  
140 them to the exhumation of source regions on the Indian plate.

### 141 **3. Sampling and Analytical Methods**

#### 142 **3.1 Sampling**

143 We sampled medium-grained sandstones from four N-S to NNE-SSW trending sections  
144 across the IBSR in central Ladakh (Figures 1A, 2A-C). These sections are: a) Temesgam (Figure  
145 2A), b) Basgo, (Figure 2A), c) Zanskar Gorge (Figure 2B) and d) Upshi-Lato (Figure 2C). We

146 collected eight samples from the Zanskar Gorge for ZFT analyses (Figure 2B). Low yield of good  
147 quality dateable apatite in most samples and zircon in several samples limited our AHe (two  
148 samples; Figures 2A, 2C) and ZHe datasets (six samples; Figures 2A-C).

149 Zircon and apatite concentrates were separated from each 8-10 kg sample using  
150 conventional mineral separation techniques involving a rock crusher, water table, Frantz magnetic  
151 separator and heavy liquids. Only samples DZA23TM from the Temesgam Formation (Figure 2A)  
152 and DZA08UL (Figure 2C) from the Lower Upshi Formation produced apatites suitable for AHe  
153 dating. Zircon yield in sample DZA08UL was low.

### 154 3.2. Zircon fission-track thermochronology

155 The zircons were mounted, polished and etched with KOH–NaOH at 220 °C for 12–36  
156 hours following standard procedures of the London Fission Track Research Group. Mounts were  
157 then irradiated with muscovite external detectors and dosimeter glass CN-5 and CN-2 at the  
158 thermal neutron facility of the Risø reactor, Denmark. Fission-track densities were measured using  
159 an optical microscope at 1250x magnification with an oil objective. Ages ( $\pm 1\sigma$ ) were calibrated by  
160 the zeta method (Hurford and Green, 1983), using a zeta factor of  $127 \pm 5$  that was determined  
161 from multiple analyses of zircon standards following the recommendations of Hurford (1990).

162 ZFT ages indicate cooling through the  $240 \pm 40$  °C temperature window depending on their  
163 U-concentrations (Hurford, 1986). Ideally, if all the ZFT ages are younger or older than  
164 depositional age of the basin, they indicate cooling in the basin or source, respectively. A mixture  
165 of older and younger ages, spanning pre- and post-deposition ages, likely suggests a case of partial  
166 fission-track annealing (or partial resetting) in zircon that indicates basin temperatures were within



167 240±40 °C. Partial annealing of zircon fission tracks begin at ~185–200 °C and the annealing is  
168 complete above ~280–300 °C (Bernet and Garver, 2005).

### 169 3.3 (U-Th)/He Zircon and Apatite Thermochronology

170 At the Arizona Radiogenic Helium Dating Laboratory, 3–5 mostly inclusion-free zircon  
171 and apatite grains with angular crystal faces were hand-picked from each sample (if available) and  
172 packed into Nb tubes. Applying the standard procedures of He extraction using coupled laser  
173 heating, the He content was measured on a quadrupole mass spectrometer, and subsequently Th  
174 and U contents were measured using ICP-MS following the methods of Reiners (2005). Raw ages  
175 were obtained by solving the combined radioactive decay-diffusion equation with known  
176 analytical concentrations of U, Th and He. These raw ages were then corrected by applying the  
177 alpha-ejection protocols of Farley et al. (1996). If the ZHe and AHe ages are younger than the  
178 depositional age of the formation, this implies basin burial temperatures of >140–200 °C and >40–  
179 90 °C, respectively, and the ages are interpreted as thermally reset. ZHe or AHe ages that are older  
180 than the depositional age of the sample are unreset and reflect cooling of the source before  
181 deposition.

### 182 3.4 Thermal Modeling

183 The ZHe and AHe ages from each sample were inverse modelled in the thermal modeling  
184 program HeFTy v.1.9.1 (Ketcham, 2005) to determine the time-Temperature ( $t$ - $T$ ) paths using the  
185 diffusion model of Guenther et al. (2013). The forward model in HeFTy predicts the expected  
186 grain age data distribution for a given  $t$ - $T$  path. The inverse algorithm solves for a family of  $t$ - $T$   
187 paths that a sample could have experienced for a fixed input dataset that include cooling ages, U-  
188 Th-Sm concentrations, grain size and zonation parameters. For each resultant  $t$ - $T$  path, HeFTy

189 calculates the statistical fit between measured and the predicted cooling ages. Acceptable-fit paths  
190 have a Kolmogorov-Smirnov probability  $\geq 0.05$ , while good-fit paths have a Kolmogorov-Smirnov  
191 probability  $\geq 0.5$ . A weighted mean path and a best-fit  $t$ - $T$  path are also generated from the  
192 inversion process. The weighted mean path is an overall summary of the inversion process with  
193 weights based on goodness of fit statistics associated with the acceptable and good-fit paths; it may  
194 or may not have an acceptable or a good fit to the data. The best-fit path has the highest goodness  
195 of fit and represents the most reasonable thermal history of a sample under the assigned constraints.

#### 196 **4. Results**

197 Our ZFT, ZHe, and AHe results are summarized in Table 2 and Figure 3 (data available in  
198 the supporting information, Tables S1–S3). All ages are reported at  $1\sigma$  uncertainty level. For  
199 previous studies that used the youngest single grain age (e.g., youngest single detrital zircon or  
200 muscovite grain age) to constrain the maximum depositional ages (MDAs) of a unit, we  
201 recalculated the MDA by estimating the weighted mean age of the youngest cluster with  
202 overlapping uncertainties (i.e.,  $YC1\sigma(2+)$  and  $YC2\sigma(3+)$  ages; Table 2, Dickinson and Gehrels,  
203 2009). If true depositional age (e.g., biostratigraphic or geochronologic tuff ages) is not available  
204 for a formation, the  $YC2\sigma(3+)$  age is adopted as a conservative estimate of its MDA (Coutts et al.,  
205 2019). Therefore, unless specified, a MDA reported in this study refers to the  $YC2\sigma(3+)$  age,  
206 which is the weighted mean age of the youngest cluster of 3 or more grains with overlapping  $2\sigma$   
207 uncertainties.

208 The individual ZFT ages span from Cretaceous to Middle Miocene time,  $182.15 \pm 50.20$  –  
209  $13.95 \pm 2.98$  Ma. Although the objective was to date 50–100 grains per sample for ZFT, low yield  
210 of zircon resulted in 17–65 grains per sample. All eight samples from the Zanskar Gorge (Figures

211 2B, 3A) fail the  $\chi^2$  test ( $P(\chi^2) < 5\%$ ) indicating the presence of some overdispersion amongst the  
212 population of measured grain ages. However, levels of overdispersion expressed as % dispersion  
213 of the central age are not always high, suggesting that in some cases, the overdispersion is not  
214 significant or poorly developed in terms of defining discrete age components. The ZFT data were  
215 decomposed into statistical grain-age components or modes using RadialPlotter (Vermeesch,  
216 2009; Table 2); however, these do not necessarily capture the true age modes if represented by  
217 only a few grains. In some cases, a few higher precision ages may be identified as an age mode  
218 rather than a population of grains that capture the true Poisson age distribution. To help determine  
219 the significance of the component ages, the data are also plotted as Abanico diagrams that combine  
220 a radial plot and a probability density estimate (supporting information, Figure S1). These plots  
221 help to visualize the distribution of ages in each sample in terms of age modes or groups, like the  
222 youngest age mode, the secondary age mode and the oldest age mode.

223 The individual ZHe ages are all Miocene,  $19.04 \pm 0.54 - 8.57 \pm 0.11$  Ma (Table 2, Figure  
224 3B). The AHe ages range from Late Miocene–Pliocene,  $6.77 \pm 0.40 - 3.94 \pm 0.17$  Ma (Table 2,  
225 Figure 3B).

## 226 **5. Interpretations**

### 227 5.1 Tar Group and Lato Formation

228 The Tar Group, which has a biostratigraphically-determined depositional age limit of ~55–  
229 50 Ma (Green et al., 2008; Henderson et al., 2010), is partially reset with respect to the ZFT system,  
230 with ages from Zanskar Gorge yielding  $130.92 \pm 31.87$  to  $21.53 \pm 4.61$  Ma for the lowermost  
231 Jurutze Formation (sample ZG45),  $76.79 \pm 14.40$  to  $13.95 \pm 2.98$  Ma for the Chogdo Formation  
232 (sample ZG55) in the middle, and  $182.15 \pm 50.20$  to  $22.60 \pm 4.57$  Ma for the topmost Nummulitic

233 Limestone Formation (sample ZG62). The zircon populations (or modes), which are younger than  
234 the depositional ages in Chogdo (ZG55) and Nummulitic Limestone (ZG62) Formations confirm  
235 partial resetting (Table 2, Figure 3A). Although sample ZG45 from the Jurutze Formation contains  
236 a single mode of  $65.2 \pm 3.1$  Ma, which is older than its  $54.7 \pm 0.3$  Ma U-Pb detrital zircon MDA  
237 (Table 2), this ZFT age likely reflects partial resetting within the PAZ whereby the older, inherited  
238 zircons within the Jurutze Formation were not thermally reset to take them below the MDA. Our  
239 data suggest that the burial temperatures in the Tar Group exceeded the ZFT lower partial  
240 annealing temperatures of  $\sim 185$ - $200$  °C. However, basin temperatures did not exceed the higher  
241 annealing temperatures of  $\sim 280$ - $300$  °C above which ZFT ages are completely reset.

242 The ZHe ages from the Tar Group Sumdo Formation (sample DZA20ZV;  $15.42 \pm 0.20$  -  
243  $8.57 \pm 0.11$  Ma) in the Zanskar Gorge are all younger than its biostratigraphic age of  $\sim 55$ - $51$  Ma  
244 (Henderson et al., 2010), indicating post-depositional temperatures exceeded  $180$ - $200$  °C (Table  
245 2, Figure 3B). The Lato Formation (possibly Cretaceous in age) within the Upshi-Lato transect is  
246 older than the youngest units of the Tar Group and has ZHe ages (sample DZA12UL;  $12.62 \pm 0.26$   
247 -  $10.05 \pm 0.20$  Ma) that are all considerably younger than its stratigraphic age (Table 2, Figure 3B).  
248 Therefore, the Lato Formation is also reset.

## 249 5.2 Indus Group

250 In the Lower Indus Group at Zanskar Gorge, the  $50.3 \pm 3.3$  Ma ZFT modal age of the Nurla  
251 Formation (sample ZG42) is within error of its U-Pb detrital zircon MDA of  $\sim 51$  Ma (Table 2,  
252 Figure 3A; Bhattacharya et al., 2020). The Choksti Conglomerate (sample ZG38), which overlies  
253 the Nurla Formation and is the basal member of the Choksti Formation, has two ZFT modes,  $40.3$   
254  $\pm 2.1$  and  $68.6 \pm 4.1$  Ma (Table 2, Figure 3A). These two age modes are approximately equal to or  
255 older than the U-Pb detrital zircon MDA of the Choksti Formation, which is  $41.5 \pm 0.2$  Ma (Wu

256 et al., 2007). The Upper Choksti member (sample ZG30), which is the topmost member of the  
257 Choksti Formation, has four ZFT modes:  $26.6 \pm 2.2$  (M1),  $37.8 \pm 3.8$  (M2),  $49.5 \pm 4.4$  (M3) and  
258  $83 \pm 8.4$  Ma (M4; Table 2, Figure 3A). The Upper Choksti Member is stratigraphically correlatable  
259 to the Hemis and Lower Upshi Formations that have U-Pb detrital zircon MDAs of  $37.8 \pm 0.2$  and  
260  $38.3 \pm 0.2$  Ma, respectively (Table 2; Sinclair and Jaffey, 2001; Henderson et al., 2011;  
261 Bhattacharya et al., 2020). The Choksti Formation is also older than the Basgo Formation, which  
262 has a Late Oligocene biostratigraphic age (Bajpai et al., 2004; Tripathy-Lang et al., 2013). The M1  
263 mode of Upper Choksti is thus younger than its depositional age, reflecting partial resetting of  
264 sample ZG30. Interestingly, partial resetting is not detected in samples ZG42 and ZG38 from the  
265 underlying Nurla Formation and Choksti Conglomerate member. This is because these two  
266 samples probably contained older zircon populations, which remained above their corresponding  
267 MDAs, despite partial resetting. The youngest M1 mode from the Lower Nimu Formation (sample  
268 ZG21) is  $25.5 \pm 3.1$  Ma, which is younger than its  $^{40}\text{Ar}/^{39}\text{Ar}$  detrital muscovite MDA of  $32.3 \pm 0.2$   
269 Ma. In terms of true depositional age, the Lower Nimu Formation is at least older than the  
270 biostratigraphically-dated Late Oligocene Basgo Formation (Bajpai et al., 2004; Buckman et al.,  
271 2018). The M1 mode of the Lower Nimu Formation thus indicates partial resetting. The upper  
272 Indus Group Upper Nimu Formation (ZG16) is unreset, with ZFT modes older than its  
273 corresponding  $^{40}\text{Ar}/^{39}\text{Ar}$  detrital muscovite MDA of  $9.5 \pm 0.5$  Ma (Table 2, Henderson et al., 2010).  
274 Overall, like the Tar Group, the Lower Indus Group is also partially reset with respect to the ZFT  
275 system, whereas the Upper Indus Group is unreset.

276 Along the Upshi-Lato traverse, the Lower Indus Group Lower Upshi Formation (sample  
277 DZA09UL) has ZHe ages from  $17.79 \pm 0.26$  –  $13.63 \pm 0.21$  Ma (Table 2, Figure 3B). The Lower  
278 Upshi Formation and its stratigraphically correlatable Hemis Formation both have detrital zircon

279 and muscovite MDAs of ~38 Ma (Table 2; Henderson et al., 2011; Bhattacharya et al., 2020). The  
280 ZHe ages in the Lower Upshi Formation are thus younger than its inferred MDA. Along the Basgo  
281 traverse, the Lower Indus Group Basgo Formation (sample DZA07SA) ZHe ages are from  $19.04$   
282  $\pm 0.54$  –  $9.90 \pm 0.27$  Ma, which are younger than its Late Oligocene depositional age based on  
283 ostracods (Bajpai et al., 2004). From the Temesgam traverse, the Lower Indus Group Temesgam  
284 Formation (sample DZA23TM) exhibits ZHe ages from  $18.91 \pm 0.52$  –  $12.81 \pm 0.18$  Ma, which  
285 are younger than its U-Pb detrital zircon MDA of  $26.8 \pm 0.1$  Ma (Table 2; Bhattacharya et al.,  
286 2020). The AHe ages from the Lower Upshi Formation (sample DZA08UL;  $6.56 \pm 0.10$  –  $5.22 \pm$   
287  $0.30$  Ma) and the Temesgam Formation (sample DZA23TM;  $6.77 \pm 0.40$  Ma –  $3.94 \pm 0.17$  Ma)  
288 are younger than their corresponding ZHe ages (Table 2; Figure 3B).

289 All ZHe ages from the Lower Indus Group are <20 Ma. Deposition in the Lower Indus  
290 Group of central Ladakh ended by ~26–23 Ma, after which basin inversion and regional  
291 counterthrusting began at ~23–20 Ma (Clift et al., 2002; Zhou et al., 2020; Bhattacharya et al.,  
292 2020). Therefore, we interpret the ZHe and AHe ages from the Lower Indus Group formations as  
293 thermally reset. This is consistent with our earlier interpretation that the Lower Indus Group is  
294 partially reset with respect to the ZFT system, implying peak burial temperatures exceeded 185–  
295 200 °C but stayed below 280–300 °C. By contrast, the stratigraphically youngest Upper Indus  
296 Group Upper Nimu Formation yields ZHe ages (sample DZA17ZV;  $17.39 \pm 0.35$  –  $13.70 \pm 0.27$   
297 Ma) older than its corresponding  $^{40}\text{Ar}/^{39}\text{Ar}$  detrital muscovite MDA of  $9.5 \pm 0.5$  Ma (Henderson  
298 et al., 2010). The Upper Indus Group is therefore unreset with respect to the ZHe system (Table 2,  
299 Figure 3B).

300 No correlation exists between ZHe or AHe ages and grain size in individual samples.  
301 However, compilation of all the ZHe ages reveals a moderate positive correlation between age and

302 grain size, which may contribute to the inter-sample ZHe age dispersion (supporting information,  
303 Figure S2). No correlation exists between AHe ages and grain size. Overall, no correlation is  
304 observed between effective uranium and ZHe or AHe ages within individual samples, or  
305 collectively (supporting information, Figure S2). This suggests radiation damage is not the primary  
306 influence of intra-sample ZHe and AHe age variability, and the distribution of ZHe ages are largely  
307 geologically controlled. The only exception is sample DZA07SA from the Basgo Formation,  
308 which shows strong negative correlation between ZHe age and effective uranium ( $R^2 = \sim 0.7$ )  
309 suggesting some control of radiation damage on the observed cooling ages (supporting  
310 information, Figure S2).

## 311 **6. Thermal modeling of (U-Th)/He cooling ages**

### 312 6.1 Modeling Strategy

313 Using our ZHe and AHe data in the thermal modeling program HeFTy, we tested two  $t$ - $T$   
314 modeling approaches to determine the cooling history of the Indus Basin rock samples. The first  
315 approach involves considering post-depositional  $t$ - $T$  constraints based on known regional geologic  
316 information, while the second approach lacks any specific post-depositional  $t$ - $T$  constraints. The  
317 purpose of testing the second approach was to check if we can reproduce near-identical cooling  
318 histories without imposing particular post-depositional  $t$ - $T$  constraints in the models, thus reducing  
319 bias.

320 Indus Basin sedimentation began in Late Cretaceous time with the deposition of the marine  
321 Tar Group, which continued until  $\sim 50$  Ma (Henderson et al., 2010). After  $\sim 50$  Ma, the continental  
322 facies of the Lower Indus Group were deposited until Late Oligocene–Early Miocene time  
323 (Sinclair and Jaffey, 2001; Clift et al., 2002; Henderson et al., 2011; Zhou et al., 2020;

324 Bhattacharya et al., 2020). The Indus Basin was inverted at ~23–20 Ma (Clift et al., 2002) and  
325 there is no prior evidence of post-depositional basin cooling. Burial temperatures largely remained  
326 below 240 °C in the Indus Basin except the Tar Group, where maximum temperatures reached 280  
327 °C (Van Haver, 1984; Clift et al., 2004). In our first approach, to fit the ZHe and AHe data in the  
328 context of known regional geologic information, we allow individual models to explore the  $t$ - $T$   
329 space younger than 23 Ma and colder than 240 or 280 °C (Figures 4A-E). We apply surface  
330 depositional temperatures of 0–25 °C and let all the models solve for  $t$ - $T$  paths from temperatures  
331 greater than the closure temperature window of the warmest thermochronometric system  
332 modelled. The ZFT, ZHe, and AHe partial annealing/retention temperatures considered are  $240 \pm$   
333  $40$  °C (Hurford, 1986), 140–200 °C (Reiners, 2005; Guenther et al., 2013), and 40–90 °C (Ehlers  
334 and Farley, 2003), respectively. Based on the knowledge of regional thermal history, a temperature  
335 constraint of 0–280 °C was applied only to the Tar Group Sumdo Formation (Sections 2.3, 6.1.2),  
336 while a 0–240 °C constraint was imposed on the  $t$ - $T$  models of the Lato, Lower Upshi, Basgo and  
337 Temesgam Formations (Sections 6.1.1, 6.1.3–6.1.5). The input  $t$ - $T$  constraints are shown by hollow  
338 rectangles in Figures 4A-E and are detailed for each formation in sections 6.1.1–6.1.5. For a given  
339 sample, simultaneous modelling of individual ZHe ages, or a mix of individual ZHe and AHe ages  
340 (2–3 grains or more), yielded no good or acceptable-fit paths with the known input data. This is a  
341 common problem with HeFTy as noted in multiple previous studies (e.g., Carrapa et al., 2014);  
342 the program could not satisfy all input parameters for a single sample simultaneously and produce  
343 acceptable results. Therefore, mean ZHe and AHe ages were calculated and incorporated as input  
344 data for  $t$ - $T$  model extraction in HeFTy using the diffusion model of Guenther et al. (2013).  
345 Inverse modeling produced a set of possible  $t$ - $T$  paths for a given sample based on the user assigned  
346  $t$ - $T$  constraints. We ran the models until at least 100 good fit  $t$ - $T$  paths were generated. The best-fit



347  $t$ - $T$  path of each model represents a statistically robust thermal history of the corresponding sample  
348 (Figures 4A-E).

349 In the second approach of  $t$ - $T$  modeling, we constrain only the depositional age of the  
350 sample and its surface depositional temperatures (0–25 °C). This approach allows HeFTy to  
351 explore maximum area in the post-depositional  $t$ - $T$  space and generate a family of  $t$ - $T$  paths that  
352 do not depend on known geologic information from the region. Similar to first approach, at least  
353 100 good fit  $t$ - $T$  paths were produced (supporting information, Figure S3). Although the best-fit  $t$ -  
354  $T$  paths from our second approach show cooling beginning approximately within the same age  
355 range as in the first approach, not all the resultant  $t$ - $T$  paths yield a geologically meaningful thermal  
356 history. Several acceptable and good-fit paths demonstrate  $t$ - $T$  histories that are unrealistic  
357 considering the available data on the timing of basin sedimentation, burial, inversion and cooling.  
358 Thus, not all statistically acceptable or good-fit  $t$ - $T$  paths obtained in our second approach are  
359 representative of the post-depositional cooling history of the basin. We examine the causes of  
360 rejection for individual models in supporting information, Text S1. The second approach is not  
361 discussed henceforth and the following sub-sections 6.1.1-6.1.5 focus on the  $t$ - $T$  constraints  
362 imposed by regional geologic data as per the first approach.

### 363 6.1.1 Lato Formation

364 The Indian margin unit Lato Formation was deposited on the surface at 0–25 °C in possibly  
365 Cretaceous time (Figure 4A). The Lato Formation is speculated to be correlatable to the Mesozoic  
366 Lamayuru Complex or the Mesozoic Chilling Formation in the Zaskar Gorge (Henderson et al.,  
367 2011), both of which are Indian margin units that are older than Early Eocene. Henderson et al.  
368 (2011) obtained two ~51 and ~77 Ma U-Pb detrital zircon grain ages and a ~67 Ma  $^{40}\text{Ar}/^{39}\text{Ar}$   
369 detrital muscovite grain age from the Lato Formation; all other detrital grains are >350 Ma. The 3

370 youngest grain ages do not overlap within  $2\sigma$ ; therefore, instead of taking a weighted average, we  
371 consider the  $\sim 77$  Ma grain age as a conservative estimate of MDA for the Lato Formation. The  
372 Lato Formation is older than, or coeval with, the youngest Tar Group units that were deposited  
373 between 55 and 50 Ma (Henderson et al., 2010, 2011). Therefore, in our HeFTy model, we  
374 constrain the depositional age of the Lato Formation from  $\sim 77$ –50 Ma, which is consistent with  
375 regional stratigraphic correlations.

376 Cooling is constrained through 0–240 °C after  $\sim 23$  Ma. Despite being older than the Tar  
377 Group, there is no evidence of burial temperatures exceeding 240 °C in the Lato Formation, and  
378 the depositional setting of the Lato Formation relative to Tar Group is undetermined. The Tar  
379 Group, which experienced temperatures  $>240$  °C, has blue-grey phyllite (Van Haver, 1984; Clift  
380 et al., 2002; Henderson et al., 2010) and was probably deposited just north of the Lato Formation  
381 that contains relatively unaltered sandstone.

#### 382 6.1.2 Sumdo Formation

383 The Tar Group Sumdo Formation was deposited at the surface (0–25 °C) at  $\sim 55$ –51 Ma  
384 (Figure 4B; Henderson et al., 2010). ZFT ages from the overlying Chogdo Formation and the  
385 underlying Jurutze Formation are partially reset, which suggest peak burial temperatures between  
386 200–280 °C in the Sumdo Formation. Van Haver (1984) calculated a maximum burial temperature  
387 of  $\sim 280$  °C using illite crystallinity from the overlying Nummulitic Limestone Formation.  
388 Therefore, we constrain cooling in the Sumdo Formation after 23 Ma through 0–280 °C.

#### 389 6.1.3 Lower Upshi Formation

390 The Lower Indus Group Lower Upshi Formation (Figure 4C) is correlatable to the Hemis  
391 Formation, and both have detrital zircon and muscovite MDAs of  $\sim 38$  Ma (Henderon et al., 2011;

392 Singh et al., 2015; Bhattacharya et al., 2020). The  $^{40}\text{Ar}/^{39}\text{Ar}$  detrital muscovite MDA of the Upper  
393 Upshi Formation, which overlies the Lower Upshi Formation, is  $\sim 25$  Ma (Table 2; Henderson et  
394 al., 2011). Because true depositional ages can be younger than MDAs, we relax the depositional  
395 age for the Lower Upshi Formation in our HeFTy model to be from  $\sim 38$ – $23$  Ma. The upper age of  
396  $\sim 23$  Ma is based on the  $\sim 26$ – $23$  Ma cessation of Lower Indus Group deposition in central Ladakh,  
397 after which regional counterthrusting began at  $\sim 23$ – $20$  Ma (Clift et al., 2002; Zhou et al., 2020;  
398 Bhattacharya et al., 2020). Our ZFT results indicate that the Lower Indus Group is partially reset  
399 with respect to the ZFT system, indicating peak burial temperatures  $>185$ – $200$  °C. In addition,  
400 paleo-geotemperature estimates from the Lower Indus Group based on illite crystallinity also  
401 suggest maximum burial temperatures of  $\sim 239$ °C (Schlup et al., 2003; Clift et al., 2004). Hence,  
402 we allow the model to cool through  $0$ – $240$  °C after  $\sim 23$  Ma.

#### 403 6.1.4 Basgo Formation

404 The Lower Indus Group Basgo Formation is  $\sim 10$ – $200$  m thick (Garzanti and Van Haver,  
405 1988) and is biostratigraphically dated as Late Oligocene in age (Bajpai et al., 2004). The  
406 formation has a youngest single zircon MDA of  $\sim 27$  Ma (Bhattacharya et al., 2020). The Basgo  
407 Formation is conformably overlain by the Temesgam Formation, which was deposited from  $26$ –  
408  $23$  Ma (Bhattacharya et al., 2020). In our  $t$ - $T$  model, we constrain the depositional age of the Basgo  
409 Formation at  $\sim 28$ – $26$  Ma (Figure 4D). Because Lower Indus Group temperatures did not exceed  
410  $240$  °C, we constrain model cooling through  $0$ – $240$  °C after  $\sim 23$  Ma.

#### 411 6.1.5 Temesgam Formation

412 The Lower Indus Group Temesgam Formation has a U-Pb detrital zircon MDA of  $\sim 27$  Ma  
413 and was deposited conformably on top of Basgo Formation from  $26$ – $23$  Ma (Table 2, Bhattacharya

414 et al., 2020). Therefore, in our  $t$ - $T$  model, we constrain the depositional age of the Temesgam  
415 Formation from ~26–23 Ma (Figure 4E). An upper age limit of ~23 Ma is imposed from the  
416 estimated age of inversion of the Indus Basin (Clift et al., 2002). Like other formations of the  
417 Lower Indus Group, we allow model cooling through 0–240 °C after 23 Ma.

## 418 6.2 Model Results

419 All the  $t$ - $T$  models demonstrate cooling from above or within the ZHe partial retention zone  
420 temperatures of 140–200°C through at least 100 good and  $\geq 188$  acceptable-fit paths (Figures 4A–  
421 E). The best-fit  $t$ - $T$  model paths show the onset of cooling by ~22–20 Ma in the Lower Indus Group  
422 Lower Upshi, Basgo and Temesgam Formations (Figures 4C–E), and by ~15–13 Ma in the Lato  
423 and Sumdo Formations (Figure 4A–B). It is possible that cooling may have started earlier than the  
424 time indicated by the best-fit  $t$ - $T$  paths in the Lato and Sumdo Formations as well; a number of  
425 good-fit paths in each model suggest cooling began before ~15–13 Ma (Figures 4A–B). We  
426 interpret the time of initiation of cooling along the best-fit  $t$ - $T$  path as the minimum time by which  
427 cooling was onset in the sample. The best-fit model paths for the Indian margin Lato Formation  
428 and the Tar Group Sumdo Formation, demonstrate a peak burial temperatures (235–245 °C) well  
429 exceeding the maximum ZHe partial retention zone temperature of ~200 °C, suggesting that the  
430 Lato and Sumdo Formations are reset and the ZHe ages reflect post-depositional basin cooling  
431 (Figures 4A–B). The Lower Upshi, Basgo and Temesgam Formations are likely reset as well; the  
432 best-fit  $t$ - $T$  model paths record cooling from above 170–190 °C, which indicate burial within the  
433 higher side of the ZHe partial retention zone. Our  $t$ - $T$  modeling is a consequence of using mean  
434 ages in each model. If individual ZHe ages are modelled grain by grain, it does not significantly  
435 change the results determined by using mean ages, and best-fit paths still indicate cooling  
436 beginning between ~22 and 11 Ma. In summary, the  $t$ - $T$  modeling results presented in this study

437 confirm the presence of a post-depositional cooling signal in the Indus Basin beginning at ~22–20  
438 Ma, and show that burial temperatures in the Indian margin Lato Formation, Tar Group and the  
439 Lower Indus Group exceeded 170–190 °C.

## 440 **7. Discussion**

### 441 7.1 Post-depositional Thermal Evolution of the IBSR

442 In general, the IBSR in central Ladakh, excluding the Upper Indus Group, experienced  
443 post-depositional cooling from >170–200 °C in Miocene–Pliocene time. The ZFT results suggest  
444 that post-depositional peak basin temperatures exceeded 185–200 °C in the Tar and Lower Indus  
445 Groups but stayed below 280–300 °C (Table 2). This basin heating resulted in partial resetting of  
446 the Tar and Lower Indus Group rocks with respect to the ZFT system. Our ZFT age interpretations  
447 are consistent with the 280 °C and 240 °C maximum burial temperatures of the Tar and Lower  
448 Indus Group rocks determined using illite crystallinity and/or vitrinite reflectance (Van Haver,  
449 1986; Schlup et al., 2003, Clift et al., 2004). Although best-fit (U-Th)/He  $t$ - $T$  model paths from the  
450 Lower Indus Group suggest burial temperatures of ~170–190 °C, this might be a consequence of  
451 relative extent of burial in the sampled sections. The Zanskar section, from where our ZFT samples  
452 are collected, exposes more altered sandstones (Tripathy-Lang et al., 2013) compared to the Upshi-  
453 Lato, Basgo, and Temsgam sections, from where our Lower Indus Group ZHe and/or AHe samples  
454 are collected.

455 Our ZHe ages range between ~19 and 8 Ma (Table 2, Figure 3B); however, these ages  
456 alone cannot be used to estimate when basin cooling began. Thermal modeling results suggest that  
457 cooling initiated by ~22–20 Ma in the Lower Indus Group of the Indus Basin (Figures 4C–E) and  
458 was occurring throughout the basin by ~15–12 Ma (Figures 4A–B). The majority of the ZHe

459 cooling ages are between ~16 and 10 Ma, and all our thermal models demonstrate steady or rapid  
460 cooling through 200–140 °C between ~20 and 10 Ma (Figure 4). Therefore, we suggest that  
461 cooling largely occurred through ZHe temperatures in Early–Middle Miocene time. Cooling  
462 continued into the Pliocene time until at least ~4 Ma, which is supported by our ~7–4 Ma AHe  
463 cooling ages and model paths (Table 2, Figures 4C, E). Our interpretation expands the ~14–7 Ma  
464 post-depositional cooling phase previously identified in the Lower Indus Group using three AFT  
465 central ages (Clift et al., 2002; Schlup et al., 2003). It is also possible that the timing of initiation  
466 of cooling decreases from north to south across the basin. For example, cooling may have begun  
467 earlier in the northern Lower Indus Group Formations between ~22 and 20 Ma (Figures 4C–E),  
468 and then progressed southwards in the Tar Group and Lato Formation between ~15–12 Ma (Figures  
469 4A–B); however more low-temperature thermochronometric studies are required in the region to  
470 check for such age trends across the Indus suture. Overall, this study in the Indus Basin of central  
471 Ladakh reveals a post-depositional Miocene–Pliocene cooling phase (~22–4 Ma) that initiated at  
472 ~22–20 Ma.

473 Unreset ~17–14 Ma ZHe ages from the Pliocene Upper Nimu Formation (Table 2; Mathur,  
474 1983; Henderson, 2010) of the stratigraphically youngest Upper Indus Group indicate post-  
475 depositional basin temperatures <140 °C. The Upper Indus Group is ~1 km thick (Henderson et  
476 al., 2010). Therefore, Pliocene deposition of the Upper Indus Group did not influence the cooling  
477 of either the Tar Group or the Lower Indus Group.

## 478 7.2 Cause of Basin Burial: Sedimentation or Overthrusting

479 In the Indus Basin, peak burial temperatures exceeded 170–190 °C just before cooling  
480 began between ~22 and 20 Ma (Figure 4A–E). This requires the IBSR, excluding the Upper Indus  
481 Group, to be progressively buried by sedimentation and/or regional overthrusting. Stratigraphic

482 studies indicate at least ~4.5 km of sediment was deposited in the Indus Basin by Early Miocene  
483 time (Henderson et al., 2010; Bhattacharya et al., 2020), which suggests some of the basin heating  
484 was the result of this stratigraphic overburden (assuming a geotherm of 20–30 °C/km). We suggest  
485 that additional burial was caused by regional overthrusting associated with the GCT. Although the  
486 age of the GCT is not well constrained by geochronological methods in NW India, it is thought to  
487 have initiated in Early Miocene time at ~23–20 Ma (Sinclair and Jaffey, 2001; Clift et al., 2002;  
488 discussed in Section 2.1). Kirstein et al. (2009) support a >20 Ma age for the GCT that led to the  
489 burial of the southern edge of the Ladakh batholith. Recent studies from south Tibet also assert  
490 that the slip on the GCT initiated at ~23 Ma (Laskowski et al., 2018), and ceased by ~15 Ma in  
491 most locations (Zhang et al., 2011; Carrapa et al., 2014; Laskowski et al., 2018; Orme, 2019).

### 492 7.3 Implications and causes of cooling

493 Despite the relatively limited scope of our data, this is the first regionally extensive multi-  
494 thermochronometric study from the IBSR and reveals a post-depositional Miocene–Pliocene  
495 cooling signal along the India-Asia collision zone in NW India. Deposition continued regionally  
496 along the collision zone until Late Oligocene–Early Miocene time (~26–23 Ma; Sinclair and  
497 Jaffey, 2001; Clift et al., 2002; Zhou et al., 2020), and there is no unequivocal evidence of cooling  
498 beginning in the IBSR until ~22–20 Ma. Using the ZHe and AHe datasets, we calculate the amount  
499 of material removed since the onset of cooling at ~22–20 Ma. This requires assuming a paleo-  
500 geothermal gradient, which is challenging considering the few studies along the collision zone in  
501 NW India. Thermal modeling of ZFT and AFT ages in Kohistan, >350 km west of the study area,  
502 reveal Miocene geothermal gradients of ~40 °C/km (Zeitler, 1985). Based on the geothermal  
503 gradient calculated by Zeitler (1985), Sinclair and Jaffey (2001) bracket a 30–50 °C/km range for  
504 Miocene geothermal gradients in the Indus Basin to estimate exhumation rates of 0.10–0.40

505 mm/yr. However, a 30–50 °C/km geothermal gradient range is incompatible with recent studies  
506 from the region (e.g., Epard and Steck, 2008; Schlup et al., 2011; Langille et al., 2014; Kumar et  
507 al., 2017). Using a bootstrapping algorithm, Kumar et al. (2017) modelled a range of geothermal  
508 gradients from ~22–33 °C/km for the Early–Middle Eocene evolution of the Ladakh batholith  
509 (Figure 1A) in NW India. In the Tso Morari Complex to the south (Figure 1A), Eocene–Oligocene  
510 geothermal gradients were 18–22 °C/km, and the geothermal gradient has remained relatively  
511 unperturbed since 30 Ma (Epard and Steck, 2008; Schlup et al., 2011). East of the Tso Morari  
512 Complex, ~200 km south-east of the study area, Early Miocene geothermal gradients estimated  
513 from the Leo Pargil shear zone by analyzing the Barrovian metamorphic pressure-temperature  
514 paths vary from ~22–30 °C/km (Langille et al., 2014). Based on these neighboring geotherm  
515 estimates, we assume a Miocene geothermal gradient of ~20–30 °C/km for the Indus Basin. It is  
516 essential to note that recent works from sedimentary basins along the India-Asia collision zone in  
517 south Tibet have all considered Miocene geothermal gradients within 20–30 °C/km (e.g., Carrapa  
518 et al., 2014; Li et al., 2016; Orme, 2019; Ning et al., 2019). Assuming a geothermal gradient of  
519 20–30 °C/km, our ZHe cooling ages indicate cooling from a mean temperature of 204 °C that  
520 requires removal of at least ~7–10 km of rock since ~22 Ma.

521         A potential driver of the Miocene–Pliocene cooling is erosion by the Indus River, which  
522 has been draining the India-Asia collision zone in NW India since at least Late Oligocene–Early  
523 Miocene time (Sinclair and Jaffey, 2001; Henderson et al., 2010, 2011; Bhattacharya et al., 2020).  
524 Indus River erosion removed the GCT-overthrust rocks that buried the Indus Basin, thereby  
525 resulting in the observed Miocene–Pliocene cooling. Although Indus River erosion played an  
526 important role in removing rocks from the India-Asia collision zone in Miocene–Pliocene time  
527 (e.g., Sinclair and Jaffey, 2001; Henderson et al., 2010), we cannot be certain that the river erosion



528 was the primary factor triggering the onset of cooling between ~22 and 20 Ma. There is  
529 considerable debate as to whether the Indus River's flow along the suture zone began in NW India  
530 in Early Eocene or Early Miocene time (Searle et al., 1996; Sinclair and Jaffey, 2001; Clift et al.,  
531 2002; Najman, 2006; Henderson et al., 2010; 2011; Zhuang et al., 2015). If the Indus River first  
532 flowed along the suture zone in the Early Miocene, aggressive erosion resulting from its initiation  
533 may explain the onset of regional cooling. If the Indus River existed at this location since Early  
534 Eocene time, additional tectonic, geodynamic and geomorphological factors were also responsible  
535 for the initiation of cooling. Interestingly, along the Yarlung suture of the India-Asia collision zone  
536 in south Tibet, a regional Miocene cooling signal from ~21–7 Ma is well documented from low-  
537 temperature thermochronometric studies (e.g., Carrapa et al., 2014; Tremblay et al., 2015, Li et  
538 al., 2015, 2016, 2017; Ge et al., 2017; Orme, 2019). These studies generally attribute the Miocene  
539 cooling signal to GCT activity and/or Yarlung River erosion (Carrapa et al., 2014; Li et al., 2015,  
540 2016, 2017; Ge et al., 2017; Orme, 2019), or intensification of Asian monsoon (Carrapa et al.,  
541 2014), while considering the regional uplift caused by the northward underthrusting of the Indian  
542 plate following Greater Indian slab break-off in Early Miocene time (DeCelles et al., 2011; Webb  
543 et al., 2017). Therefore, it is possible that a similar combination of tectonic, geodynamic, and  
544 geomorphologic factors resulted in a tectonic setting that facilitated regional cooling along the  
545 India-Asia collision zone in NW India. However, given the limited previously published and new  
546 data in this region, it is difficult to test such scenarios. This study therefore provides the foundation  
547 to investigate more complex tectono-thermal events in the India-Asia collision zone of NW India  
548 and test models that correlate them with the results from south Tibet.

## 549 **8. Conclusions**

550 Low-temperature thermochronology of the Indus Basin in central Ladakh reveals a post-  
551 depositional Miocene–Pliocene (~22–4 Ma) cooling history. Our ZFT and ZHe results confirm  
552 that the basin was buried to temperatures >170–200 °C and exceeded 240 °C in the deepest  
553 formations. Basin burial is attributed to sedimentation and regional northward counterthrusting by  
554 the GCT in Early Miocene time. Thermal modeling of ZHe and AHe ages indicate cooling onset  
555 by ~22–20 Ma, occurred rapidly or steadily across the basin through ZHe partial retention zone  
556 temperatures between ~20 and 10 Ma, and continued at least until ~4 Ma. This Miocene–Pliocene  
557 cooling, which removed ~7–10 km of rock from the India-Asia collision zone, may be linked to  
558 erosion by the Indus River that dissects the ISBR. However, more low-temperature  
559 thermochronometric data from western and eastern Ladakh are required to confirm if this cooling  
560 signal is present along the strike of the India-Asia collision zone in NW India, as documented in  
561 south Tibet. If a regional Miocene–Pliocene cooling signal is indeed present both in NW India and  
562 south Tibet, it might be indicative of a continental-scale thermal event operating along the India-  
563 Asia collision zone driven by a combination of tectonic, geodynamic, and geomorphologic factors  
564 rather than Indus river incision alone.

## 565 **Acknowledgements**

566 We thank the Editor-in-Chief, Dr. Taylor Schildgen for editorial handling and valuable  
567 feedback. Constructive reviews from Dr. Jean-Luc Epard and Dr. Ryan Leary greatly improved  
568 the manuscript. All thermochronological data are available in the Supporting Information file and  
569 can also be accessed at the 4TU.Centre for Research Data Repository via doi: 10.4121/12771332.  
570 Student travel grants to GB by the Geological Society of America and The University of Alabama  
571 funded the fieldwork for this research. Uttam Chowdhury, Erin Abel and Peter Reiners at the  
572 Arizona Radiogenic Helium Dating Laboratory, The University of Arizona, assisted GB with the

- 573 He-analyses. Talat Ahmad, University of Kashmir helped with procuring permits for fieldwork.
- 574 Konchok Dorjay provided logistical support to GB in extreme weather conditions.

575 **References**

- 576 Ahmad, T., Tanaka, T., Sachan, H. K., Asahara, Y., Islam, R., & Khanna, P. P. (2008).  
577 Geochemical and isotopic constraints on the age and origin of the Nidar Ophiolitic  
578 Complex, Ladakh, India: Implications for the Neo-Tethyan subduction along the Indus  
579 suture zone. *Tectonophysics*, 451(1-4), 206-224.  
580 <https://doi.org/10.1016/j.tecto.2007.11.049>
- 581 Bajpai, S., Whatley, R. C., Prasad, G. V. R., & Whittaker, J. E. (2004). An Oligocene non-  
582 marine ostracod fauna from the Basgo Formation (Ladakh Molasse), NW Himalaya,  
583 India. *Journal of Micropalaeontology*, 23(1), 3-9. <https://doi.org/10.1144/jm.23.1.3>
- 584 Bhattacharya, G., Robinson, D. M., Wielicki, M.M. (2020). Detrital zircon provenance of the  
585 Indus Group, Ladakh, NW India: Implications for the timing of India-Asia collision and  
586 other syn-orogenic processes. *Geological Society of America Bulletin* (Accepted, in copy-  
587 editing)
- 588 Bernet, M., & Garver, J. I. (2005). Fission-track analysis of detrital zircon. *Reviews in*  
589 *Mineralogy and Geochemistry*, 58(1), 205-237. <https://doi.org/10.2138/rmg.2005.58.8>
- 590 Brookfield, M., & Andrews-Speed, C. (1984). Sedimentology, petrography and tectonic  
591 significance of the shelf, flysch and molasse clastic deposits across the Indus suture zone,  
592 Ladakh, NW India. *Sedimentary Geology*, 40(4), 249-286. [https://doi.org/10.1016/0037-  
593 0738\(84\)90011-3](https://doi.org/10.1016/0037-0738(84)90011-3)
- 594 Buchs, N., & Epard, J.-L. (2018). Geology of the eastern part of the Tso Morari nappe, the Nidar  
595 Ophiolite and the surrounding tectonic units (NW Himalaya, India). *Journal of Maps*,  
596 15(2), 38-48. <https://doi.org/10.1080/17445647.2018.1541196>
- 597 Buckman, S., Aitchison, J. C., Nutman, A. P., Bennett, V. C., Saktura, W. M., Walsh, J. M. J., . .  
598 . Hidaka, H. (2018). The Spongtang Massif in Ladakh, NW Himalaya: An Early  
599 Cretaceous record of spontaneous, intra-oceanic subduction initiation in the Neotethys.  
600 *Gondwana Research*, 63, 226-249. <https://doi.org/10.1016/j.gr.2018.07.003>
- 601 Carrapa, B., Orme, D., DeCelles, P. G., Kapp, P., Cosca, M. A., & Waldrip, R. (2014). Miocene  
602 burial and exhumation of the India-Asia collision zone in southern Tibet: Response to  
603 slab dynamics and erosion. *Geology*, 42(5), 443-446. <https://doi.org/10.1130/G35350.1>
- 604 Clift, P., Schlup, M., Carter, A., & Steck, A. (2004). Discussion of exhumation history of eastern  
605 Ladakh revealed by <sup>40</sup>Ar/<sup>39</sup>Ar and fission track ages: the Indus River–Tso Morari  
606 transect, NW Himalaya. *Journal of the Geological Society*, 161(5), 893-894.  
607 <https://doi.org/10.1144/0016-764903-104>
- 608 Clift, P. D., Carter, A., Krol, M., & Kirby, E. (2002). Constraints on India-Eurasia collision in  
609 the Arabian Sea region taken from the Indus Group, Ladakh Himalaya, India. In P. D.  
610 Clift, D. Kroon, C. Gaedicke, & J. Craig (Eds.), *The Tectonic and Climatic Evolution of*  
611 *the Arabian Sea Region: Geological Society, London, Special Publication 195* (pp. 97-

- 612 116). <https://doi.org/10.1144/gsl.Sp.2002.195.01.07>
- 613 Coutts, D. S., Matthews, W. A., & Hubbard, S. M. (2019). Assessment of widely used methods  
614 to derive depositional ages from detrital zircon populations. *Geoscience Frontiers*, 10(4),  
615 1421-1435. <https://doi.org/10.1016/j.gsf.2018.11.002>
- 616 Das, S., Basu, A. R., Mukherjee, B. K., Marcantonio, F., Sen, K., Bhattacharya, S., & Gregory,  
617 R. T. (2020). Origin of Indus ophiolite-hosted ophicarbonates: Isotopic evidence of  
618 mixing between seawater and continental crust-derived fluid during Neo-Tethys closure.  
619 *Chemical Geology*, 551, 119772.  
620 <https://doi.org/https://doi.org/10.1016/j.chemgeo.2020.119772>
- 621 DeCelles, P. G., Kapp, P., Quade, J., & Gehrels, G. E. (2011). Oligocene-Miocene Kailas basin,  
622 southwestern Tibet: Record of postcollisional upper-plate extension in the Indus-Yarlung  
623 suture zone. *Geological Society of America Bulletin*, 123(7-8), 1337-1362.  
624 <https://doi.org/10.1130/b30258.1>
- 625 Dickinson, W. R., & Gehrels, G. E. (2009). Use of U–Pb ages of detrital zircons to infer  
626 maximum depositional ages of strata: A test against a Colorado Plateau Mesozoic  
627 database. *Earth and Planetary Science Letters*, 288(1-2), 115-125.  
628 <https://doi.org/10.1016/j.epsl.2009.09.013>
- 629 Dumitru, T. A. (1991). Effects of subduction parameters on geothermal gradients in forearcs,  
630 with an application to Franciscan Subduction in California. *Journal of Geophysical*  
631 *Research: Solid Earth*, 96(B1), 621-641. <https://doi.org/10.1029/90jb01913>
- 632 Ehlers, T. A., & Farley, K. A. (2003). Apatite (U–Th)/He thermochronometry: methods and  
633 applications to problems in tectonic and surface processes. *Earth and Planetary Science*  
634 *Letters*, 206(1-2), 1-14. [https://doi.org/10.1016/S0012-821X\(02\)01069-5](https://doi.org/10.1016/S0012-821X(02)01069-5)
- 635 Epard, J.-L., & Steck, A. (2008). Structural development of the Tso Moriri ultra-high pressure  
636 nappe of the Ladakh Himalaya. *Tectonophysics*, 451(1-4), 242-264.  
637 <https://doi.org/10.1016/j.tecto.2007.11.050>
- 638 Farley, K., Wolf, R., & Silver, L. (1996). The effects of long alpha-stopping distances on (U  
639 Th)/He ages. *Geochimica et cosmochimica acta*, 60(21), 4223-4229.  
640 [https://doi.org/10.1016/S0016-7037\(96\)00193-7](https://doi.org/10.1016/S0016-7037(96)00193-7)
- 641 Garzanti, E., Baud, A., & Mascle, G. (1987). Sedimentary record of the northward flight of India  
642 and its collision with Eurasia (Ladakh Himalaya, India). *Geodinamica Acta*, 1(4/5), 297-  
643 312. <https://doi.org/10.1080/09853111.1987.11105147>
- 644 Garzanti, E., & Van Haver, T. (1988). The Indus clastics: forearc basin sedimentation in the  
645 Ladakh Himalaya (India). *Sedimentary Geology*, 59(3-4), 237-249.  
646 [https://doi.org/10.1016/0037-0738\(88\)90078-4](https://doi.org/10.1016/0037-0738(88)90078-4)
- 647 Ge, Y.-K., Dai, J.-G., Wang, C.-S., Li, Y.-L., Xu, G.-Q., & Danisik, M. (2017). Cenozoic  
648 thermo-tectonic evolution of the Gangdese batholith constrained by low-temperature

- 649 thermochemistry. *Gondwana Research*, 41, 451-462.  
650 <https://doi.org/10.1016/j.gr.2016.05.006>
- 651 Green, O. R., Searle, M. P., Corfield, R. I., & Corfield, R. M. (2008). Cretaceous-Tertiary  
652 Carbonate Platform Evolution and the Age of the India-Asia Collision along the Ladakh  
653 Himalaya (Northwest India). *The Journal of Geology*, 116(4), 331-353.  
654 <https://doi.org/10.1086/588831>
- 655 Guenther, W. R., Reiners, P. W., Ketcham, R. A., Nasdala, L., & Giester, G. (2013). Helium  
656 diffusion in natural zircon: Radiation damage, anisotropy, and the interpretation of zircon  
657 (U-Th)/He thermochronology. *American Journal of Science*, 313(3), 145-198.  
658 <https://doi.org/10.2475/03.2013.01>
- 659 Henderson, A. L., Najman, Y., Parrish, R., BouDagher-Fadel, M., Barford, D., Garzanti, E., &  
660 Andò, S. (2010). Geology of the Cenozoic Indus Basin sedimentary rocks:  
661 Paleoenvironmental interpretation of sedimentation from the western Himalaya during  
662 the early phases of India-Eurasia collision. *Tectonics*, 29(6), n/a-n/a.  
663 <https://doi.org/10.1029/2009tc002651>
- 664 Henderson, A. L., Najman, Y., Parrish, R., Mark, D. F., & Foster, G. L. (2011). Constraints to  
665 the timing of India–Eurasia collision; a re-evaluation of evidence from the Indus Basin  
666 sedimentary rocks of the Indus–Tsangpo Suture Zone, Ladakh, India. *Earth-Science  
667 Reviews*, 106(3-4), 265-292. <https://doi.org/10.1016/j.earscirev.2011.02.006>
- 668 Hurford, A. J. (1986). Cooling and uplift patterns in the Lepontine Alps South Central  
669 Switzerland and an age of vertical movement on the Insubric fault line. *Contributions to  
670 Mineralogy and Petrology*, 92(4), 413-427. <https://doi.org/10.1007/BF00374424>
- 671 Hurford, A. J. (1990). Standardization of fission track dating calibration: Recommendation by  
672 the Fission Track Working Group of the I.U.G.S. Subcommittee on Geochronology.  
673 *Chemical Geology: Isotope Geoscience section*, 80(2), 171-178.  
674 [https://doi.org/10.1016/0168-9622\(90\)90025-8](https://doi.org/10.1016/0168-9622(90)90025-8)
- 675 Hurford, A. J., & Green, P. F. (1983). The zeta age calibration of fission-track dating. *Chemical  
676 Geology*, 41, 285-317. [https://doi.org/10.1016/S0009-2541\(83\)80026-6](https://doi.org/10.1016/S0009-2541(83)80026-6)
- 677 Kapp, P., & DeCelles, P. G. (2019). Mesozoic–Cenozoic geological evolution of the Himalayan-  
678 Tibetan orogen and working tectonic hypotheses. *American Journal of Science*, 319(3),  
679 159-254. <https://doi.org/10.2475/03.2019.01>
- 680 Ketcham, R. A. (2005). Forward and Inverse Modeling of Low-Temperature  
681 Thermochronometry Data. *Reviews in Mineralogy and Geochemistry*, 58(1), 275-314.  
682 doi: <https://doi.org/10.2138/rmg.2005.58.11>
- 683 Kirstein, L. A., Foeken, J. P. T., van der Beek, P., Stuart, F. M., & Phillips, R. J. (2009).  
684 Cenozoic unroofing history of the Ladakh Batholith, western Himalaya, constrained by  
685 thermochronology and numerical modelling. *Journal of the Geological Society*, 166(4),  
686 667-678. <https://doi.org/10.1144/0016-76492008-107>

- 687 Kirstein, L. A., Sinclair, H., Stuart, F. M., & Dobson, K. (2006). Rapid early Miocene  
688 exhumation of the Ladakh batholith, western Himalaya. *Geology*, 34(12).  
689 <https://doi.org/10.1130/g22857a.1>
- 690 Kumar, R., Jain, A., Lal, N., & Singh, S. (2017). Early–Middle Eocene exhumation of the Trans-  
691 Himalayan Ladakh Batholith, and the India–Asia convergence. *CURRENT SCIENCE*,  
692 113(6), 1090.
- 693 Langille, J. M., Jessup, M. J., Cottle, J., & Ahmad, T. (2014). Kinematic and thermal studies of  
694 the Leo Pargil Dome: Implications for synconvergent extension in the NW Indian  
695 Himalaya. *Tectonics*, 33(9), 1766-1786. <https://doi.org/10.1002/2014tc003593>
- 696 Laskowski, A. K., Kapp, P., & Cai, F. (2018). Gangdese culmination model: Oligocene–Miocene  
697 duplexing along the India-Asia suture zone, Lazi region, southern Tibet. *GSA Bulletin*,  
698 130(7-8), 1355-1376. <https://doi.org/10.1130/b31834.1>
- 699 Li, G., Kohn, B., Sandiford, M., & Xu, Z. (2017). India-Asia convergence: Insights from burial  
700 and exhumation of the Xigaze fore-arc basin, south Tibet. *Journal of Geophysical*  
701 *Research: Solid Earth*, 122(5), 3430-3449. <https://doi.org/10.1002/2017jb014080>
- 702 Li, G., Kohn, B., Sandiford, M., Xu, Z., Tian, Y., & Seiler, C. (2016). Synorogenic  
703 morphotectonic evolution of the Gangdese batholith, South Tibet: Insights from low-  
704 temperature thermochronology. *Geochemistry, Geophysics, Geosystems*, 17(1), 101-112.  
705 <https://doi.org/10.1002/2015gc006047>
- 706 Li, G., Tian, Y., Kohn, B. P., Sandiford, M., Xu, Z., & Cai, Z. (2015). Cenozoic low temperature  
707 cooling history of the Northern Tethyan Himalaya in Zedang, SE Tibet and its  
708 implications. *Tectonophysics*, 643, 80-93. <https://doi.org/10.1016/j.tecto.2014.12.014>
- 709 Mathur, N. (1983). The Indus Formation of the Ladakh Himalaya: its biozonation, correlation  
710 and faunal provincialism. In (eds) Thakur, V.C. & Sharma, K.K. (Eds.), *Geology of Indus*  
711 *Suture Zone of Ladakh: Professor DN Wadia Birth Centenary Commemorative Volume*.  
712 *Wadia Institute of Himalayan Geology*, (pp. 127-144).
- 713 Najman, Y. (2006). The detrital record of orogenesis: A review of approaches and techniques  
714 used in the Himalayan sedimentary basins. *Earth-Science Reviews*.  
715 <https://doi.org/10.1016/j.earscirev.2005.04.004>
- 716 Ning, Z., Zhang, L., Huntington, K. W., Wang, C., Dai, J., Han, Z., . . . Zhang, J. (2019). The  
717 burial and exhumation history of the Liuqu Conglomerate in the Yarlung Zangbo suture  
718 zone, southern Tibet: Insights from clumped isotope thermometry. *Journal of Asian*  
719 *Earth Sciences*, 174, 205-217. <https://doi.org/10.1016/j.jseas.2018.12.009>
- 720 Orme, D. A. (2019). Burial and exhumation history of the Xigaze forearc basin, Yarlung suture  
721 zone, Tibet. *Geoscience Frontiers*, 10(3), 895-908.  
722 <https://doi.org/10.1016/j.gsf.2017.11.011>
- 723 Reiners, P. W. (2005). Zircon (U-Th)/He Thermochronometry. *Reviews in Mineralogy and*

- 724 Geochemistry, 58(1), 151-179. doi: <https://doi.org/10.2138/rmg.2005.58.6>
- 725 Robertson, A., & Sharp, I. (1998). Mesozoic deep-water slope/rise sedimentation and volcanism  
726 along the North-Indian passive margin: evidence from the Karamba Complex, Indus  
727 suture zone (Western Ladakh Himalaya). *Journal of Asian Earth Sciences*, 16(2-3), 195-  
728 215. [https://doi.org/10.1016/S0743-9547\(98\)00010-5](https://doi.org/10.1016/S0743-9547(98)00010-5)
- 729 Schlup, M., Carter, A., Cosca, M., & Steck, A. (2003). Exhumation history of eastern Ladakh  
730 revealed by 40Ar/39Ar and fission-track ages: the Indus River–Tso Morari transect, NW  
731 Himalaya. *Journal of the Geological Society*, 160(3), 385-399.  
732 <https://doi.org/10.1144/0016-764902-084>
- 733 Schlup, M., Steck, A., Carter, A., Cosca, M., Epard, J.-L., & Hunziker, J. (2011). Exhumation  
734 history of the NW Indian Himalaya revealed by fission track and 40Ar/39Ar ages.  
735 *Journal of Asian Earth Sciences*, 40(1), 334-350.  
736 <https://doi.org/10.1016/j.jseaes.2010.06.008>
- 737 Searle, M., Corfield, R. I., Stephenson, B., & McCarron, J. (1997). Structure of the North Indian  
738 continental margin in the Ladakh–Zaskar Himalayas: implications for the timing of  
739 obduction of the Spontang ophiolite, India–Asia collision and deformation events in the  
740 Himalaya. *Geological Magazine*, 134(3), 297-316.  
741 <https://doi.org/10.1017/S0016756897006857>
- 742 Searle, M. P. (1996). Geological evidence against large-scale pre-Holocene offsets along the  
743 Karakoram Fault: Implications for the limited extrusion of the Tibetan plateau. *Tectonics*,  
744 15(1), 171-186. <https://doi.org/10.1029/95tc01693>
- 745 Searle, M. P. (2019). Timing of subduction initiation, arc formation, ophiolite obduction and  
746 India–Asia collision in the Himalaya. In P. J. Treloar & M. P. Searle (Eds.), *Himalayan*  
747 *Tectonics: A Modern Synthesis: Geological Society, London, Special Publication 483*  
748 (pp. 19-37). <https://doi.org/10.1144/sp483.8>
- 749 Searle, M. P., Pickering, K. T., & Cooper, D. J. W. (1990). Restoration and evolution of the  
750 intermontane Indus molasse basin, Ladakh Himalaya, India. *Tectonophysics*, 174(3-4),  
751 301-314. [https://doi.org/10.1016/0040-1951\(90\)90327-5](https://doi.org/10.1016/0040-1951(90)90327-5)
- 752 Searle, M. P., Waters, D. J., Rex, D. C., & Wilson, R. N. (1992). Pressure, temperature and time  
753 constraints on Himalayan metamorphism from eastern Kashmir and western Zaskar.  
754 *Journal of the Geological Society*, 149(5), 753-773.  
755 <https://doi.org/10.1144/gsjgs.149.5.0753>
- 756 Sharman, G. R., Sharman, J. P., & Sylvester, Z. (2018). detritalPy: A Python-based toolset for  
757 visualizing and analysing detrital geo-thermochronologic data. *The Depositional Record*,  
758 4(2), 202-215. <https://doi.org/10.1002/dep2.45>
- 759 Sinclair, H. D., & Jaffey, N. (2001). Sedimentology of the Indus Group, Ladakh, northern India:  
760 implications for the timing of initiation of the palaeo-Indus River. *Journal of the*  
761 *Geological Society [London]*, 158(1), 151-162. <https://doi.org/10.1144/jgs.158.1.151>



- 762 Singh, I. B., Sahni, A., Jain, A. K., Upadhyay, R., Parcha, S. K., Parmar, V., . . . Ahmad, S.  
763 (2015). Post-collision sedimentation in the Indus Basin (Ladakh, India): Implications for  
764 the evolution of the northern margin of the Indian Plate. *Journal of the Palaeontological*  
765 *Society of India*, 60(2), 97-146.
- 766 Steck, A. (2003). Geology of the NW Indian Himalaya. *Ecologiae Geologicae Helvetiae*, 96, 147-  
767 196. <https://doi.org/10.1007/s00015-003-1091-4>
- 768 St-Onge, M. R., Rayner, N., & Searle, M. P. (2010). Zircon age determinations for the Ladakh  
769 batholith at Chumathang (Northwest India): Implications for the age of the India–Asia  
770 collision in the Ladakh Himalaya. *Tectonophysics*, 495(3-4), 171-183. doi:  
771 <https://doi.org/10.1016/j.tecto.2010.09.010>
- 772 Tremblay, M. M., Fox, M., Schmidt, J. L., Tripathy-Lang, A., Wielicki, M. M., Harrison, T. M., .  
773 . . Shuster, D. L. (2015). Erosion in southern Tibet shut down at approximately 10 Ma  
774 due to enhanced rock uplift within the Himalaya. *Proceedings of the National Academy*  
775 *of Sciences USA*, 112(39), 12030-12035. <https://doi.org/10.1073/pnas.1515652112>
- 776 Tripathy-Lang, A., Hodges, K. V., van Soest, M. C., & Ahmad, T. (2013). Evidence of pre-  
777 Oligocene emergence of the Indian passive margin and the timing of collision initiation  
778 between India and Eurasia. *Lithosphere*, 5(5), 501-506. <https://doi.org/10.1130/1273.1>
- 779 Van Haver, T. (1984). *Etude stratigraphique, sédimentologique et structurale d'un bassin*  
780 *d'avant arc: exemple du bassin de l'Indus, Ladakh, Himalaya*. Université Scientifique et  
781 Médicale de Grenoble. <https://tel.archives-ouvertes.fr/tel-00641418v2>
- 782 Van Haver, T., Bonhomme M. G., Mascle G., and Aprahamian J. (1986), Analyses K/Ar de  
783 phyllites fines des formations détritiques de l'Indus au Ladakh (Inde): Mise en évidence  
784 de l'âge éocène supérieur du métamorphisme. *Comptes rendus de l'Académie des*  
785 *sciences.*, Serie 2, 302(6), 325-330.
- 786 Vermeesch, P. (2009). RadialPlotter: A Java application for fission track, luminescence and other  
787 radial plots. *Radiation Measurements*, 44(4), 409-410.  
788 <https://doi.org/10.1016/j.radmeas.2009.05.003>
- 789 Walsh, J. M. J., Buckman, S., Nutman, A. P., & Zhou, R. (2019). Age and Provenance of the  
790 Nindam Formation, Ladakh, NW Himalaya: Evolution of the Intraoceanic Dras Arc  
791 Before Collision With India. *Tectonics*, 38(8), 3070-3096.  
792 <https://doi.org/10.1029/2019tc005494>
- 793 Webb, A. A. G., Guo, H., Clift, P. D., Husson, L., Müller, T., Costantino, D., . . . Wang, Q.  
794 (2017). The Himalaya in 3D: Slab dynamics controlled mountain building and monsoon  
795 intensification. *Lithosphere*. <https://doi.org/10.1130/1636.1>
- 796 Weinberg, R. F., & Dunlap, W. J. (2000). Growth and Deformation of the Ladakh Batholith,  
797 Northwest Himalayas: Implications for Timing of Continental Collision and Origin of  
798 Calc-Alkaline Batholiths. *Journal of Geology*, 108(3), 303-320.  
799 <https://doi.org/10.1086/314405>

- 800 Wu, F.-Y., Clift, P. D., & Yang, J.-H. (2007). Zircon Hf isotopic constraints on the sources of the  
801 Indus Molasse, Ladakh Himalaya, India. *Tectonics*, 26(2), TC2014  
802 <https://doi.org/10.1029/2006tc002051>
- 803 Zeitler, P. K. (1985). Cooling history of the NW Himalaya, Pakistan. *Tectonics*, 4(1), 127-151.  
804 doi: <https://doi.org/10.1029/TC004i001p00127>
- 805 Zhang, R., Murphy, M. A., Lapen, T. J., Sanchez, V., & Heizler, M. (2011). Late Eocene crustal  
806 thickening followed by Early-Late Oligocene extension along the India-Asia suture zone:  
807 Evidence for cyclicity in the Himalayan orogen. *Geosphere*, 7(5), 1249-1268.  
808 <https://doi.org/10.1130/GES00643.1>
- 809 Zhou, R., Aitchison, J. C., Lokho, K., Sobel, E. R., Feng, Y., & Zhao, J.-x. (2020). Unroofing the  
810 Ladakh Batholith: constraints from autochthonous molasse of the Indus Basin, NW  
811 Himalaya. *Journal of the Geological Society*, 177(4), 818-825.  
812 <https://doi.org/10.1144/jgs2019-188>
- 813 Zhu, C., Rao, S., & Hu, S. (2016). Application of illite crystallinity for paleo-temperature  
814 reconstruction: A case study in the western Sichuan basin, SW China. *Carpathian*  
815 *Journal of Earth and Environmental Sciences*, 11(2), 599-608.
- 816 Zhuang, G., Najman, Y., Guillot, S., Roddaz, M., Antoine, P.-O., Métais, G., . . . Solangi, S. H.  
817 (2015). Constraints on the collision and the pre-collision tectonic configuration between  
818 India and Asia from detrital geochronology, thermochronology, and geochemistry studies  
819 in the lower Indus basin, Pakistan. *Earth and Planetary Science Letters*, 432, 363-373.  
820 <https://doi.org/10.1016/j.epsl.2015.10.026>

821 **Figure Captions**

822 **Figure 1. A.** Geological map of the India-Asia collision zone in Ladakh, NW India showing major tectono-  
823 stratigraphic units modified after Buchs and Epard (2019). Studied cross-sections are indicated in red: 1 -  
824 Temesgam section; 2 - Basgo section; 3 - Zaskar Gorge; 4 - Upshi-Lato section. **B:** Location of the study  
825 area (red) with respect to major terranes of south Asia. Blackened zones contain ophiolites. **C:** Schematic  
826 cross-section along AA' through the collision zone in NW India.

827 **Figure 2.** Geological maps of **(A)** Temesgam and Basgo sections (numbered 1 and 2 in red respectively;  
828 modified after Garzanti and Van Haver, 1988; Tripathy-Lang et al., 2013), **(B)** Zaskar Gorge (modified  
829 after Henderson et al. 2010), and **(C)** Upshi-Lato section (modified after Henderson et al. 2011) showing  
830 formations, major structures and our sample locations. Abbreviations: Fm - Formation, sh - shale,  
831 Conglomerate - cgl, N lst - Nummulitic Limestone, U - upper, M - middle, L - lower, R - river.

832 **Figure 3. A.** Plot showing range of ZFT ages from the Zaskar Gorge samples. Vertical black lines specify  
833 ZFT age ranges for each sample and contain solid black diamonds that indicate corresponding depositional  
834 ages. Mean percentage of grains representing modes M1, M2, M3 and M4, determined from Abanico plots,  
835 are shown in parantheses. Abbreviations: Congl. - Conglomerate; Numm. Lst. - Nummulitic Limestone; n  
836 - number of grains. Solid black diamonds indicate depositional ages. **B.** Zircon (ZHe) and apatite (AHe)  
837 (U-Th)/He ages versus stratigraphic ages of the Indus Basin sedimentary rocks (IBSR). The ZHe ages (2-3  
838 grains per sample) of individual grains are indicated by the horizontal bars on the dark grey rectangles. The  
839 AHe ages (5 grains per sample) are represented by light grey box and whisker plots, where the whiskers  
840 represent maximum and minimum individual apatite ages. Solid black squares indicate depositional ages.  
841 \* - The depositional age of the Lato Formation is Late Cretaceous, which is not shown on the vertical scale.  
842 The depositional ages are compiled from Bajpai et al. (2004), Wu et al., (2007), Henderson et al. (2010,  
843 2011) and Bhattacharya et al. (2020).

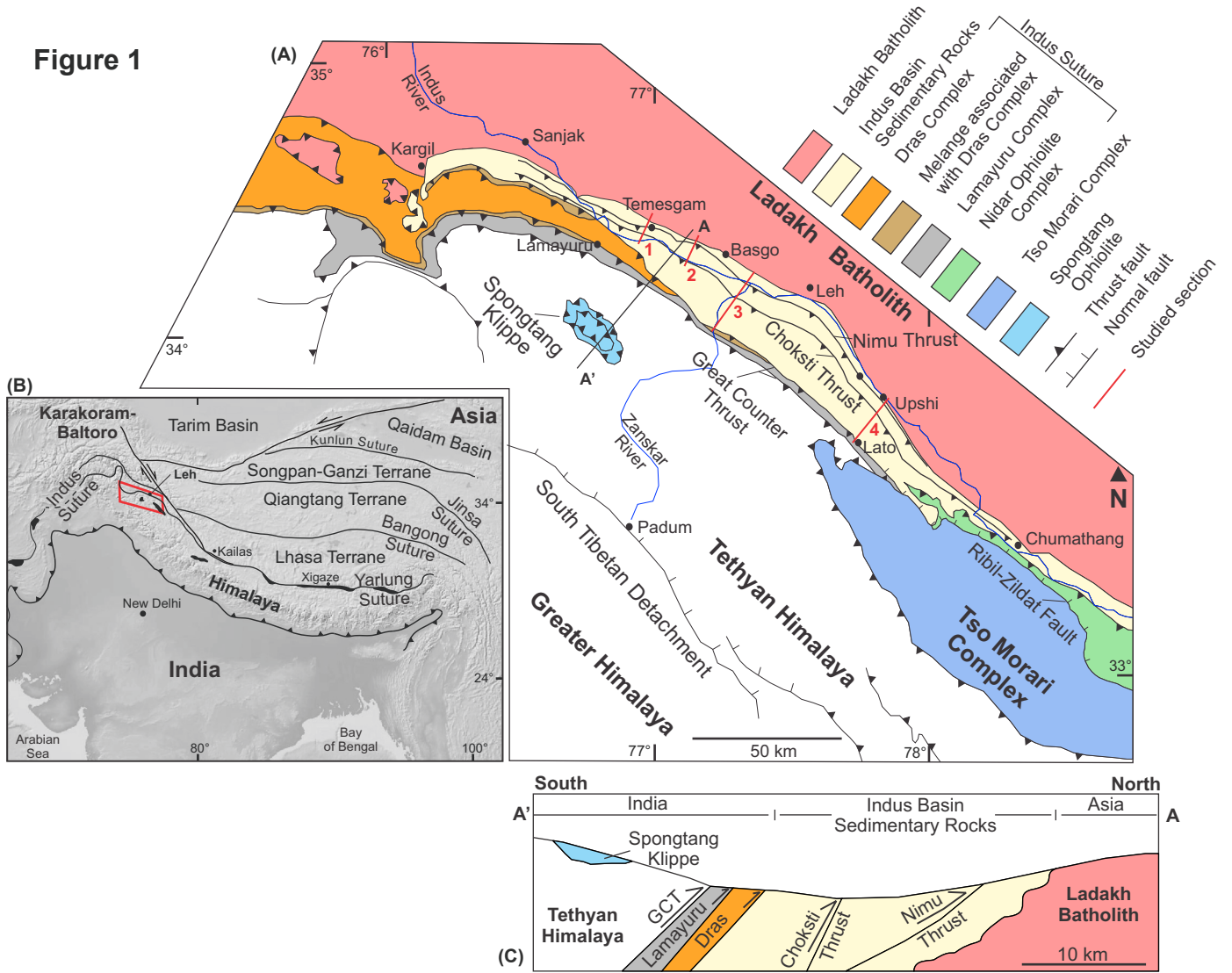
844 **Figure 4.** Time-temperature ( $t$ - $T$ ) models of the Indus Basin extracted using the HeFTy program (Ketcham,  
845 2005). **(A)** Lato Formation (Model DZA12UL), **(B)** Sumdo Formation (Model DZA20ZV), **(C)** Lower  
846 Upshi Formation (Model DZA09UL), **(D)** Basgo Formation (Model DZA07SA), and **(E)** Temesgam  
847 Formation (Model DZA23TM). Abbreviations: PT - paths tried, AP (green) -acceptable paths, GP (pink) -  
848 good paths. Solid black line indicates best fit model path. Hollow square boxes demarcate  $t$ - $T$  constraints.

849 **Table Captions**

850 **Table 1.** Published stratigraphic schemes compared across the IBSR sections in NW India.

851 **Table 2.** Summary of ZFT, ZHe and AHe ages from Zanskar Gorge, Upshi-Lato, Basgo and Temesgam  
852 sections.

**Figure 1**



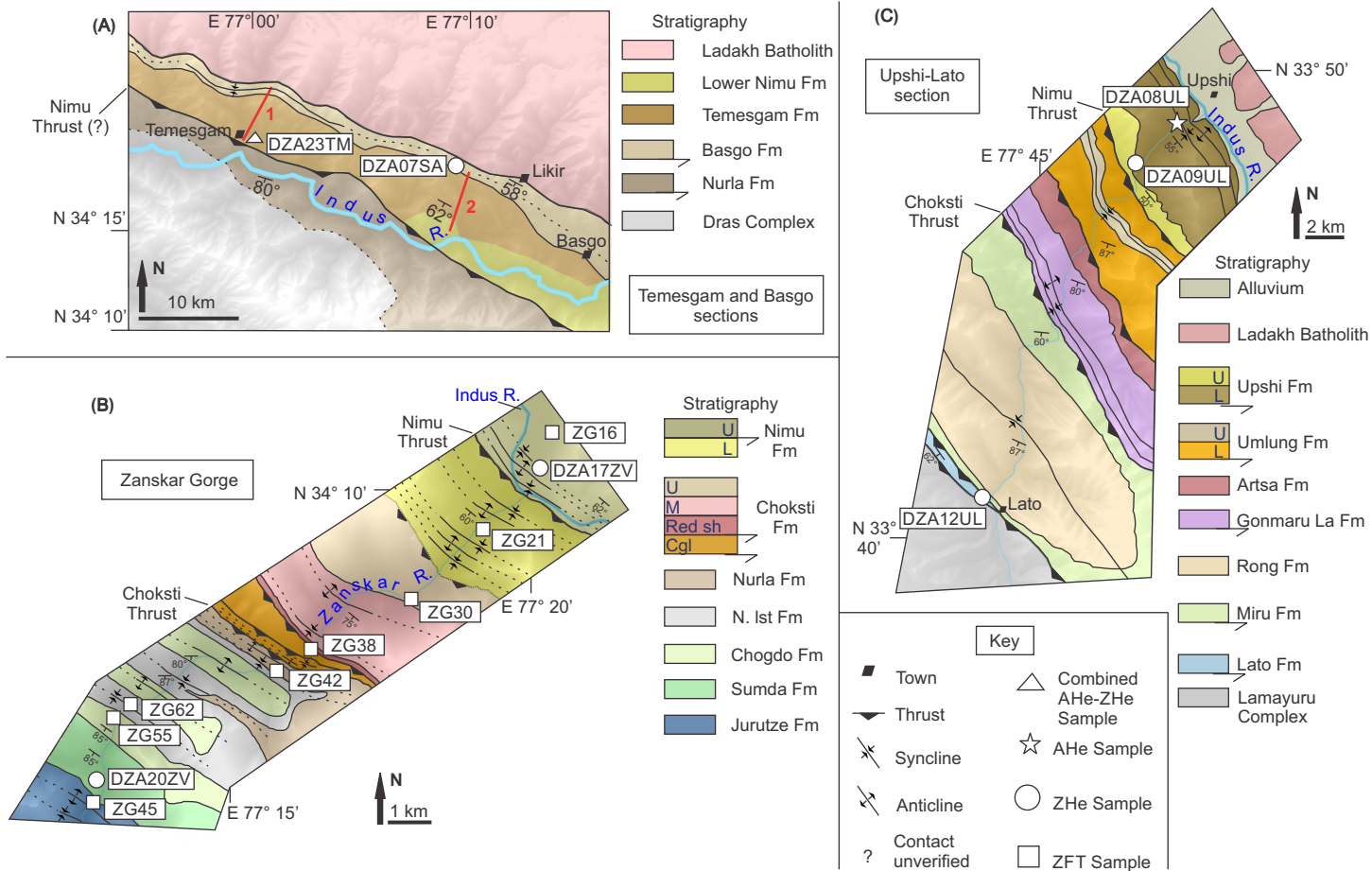


**Figure 2**

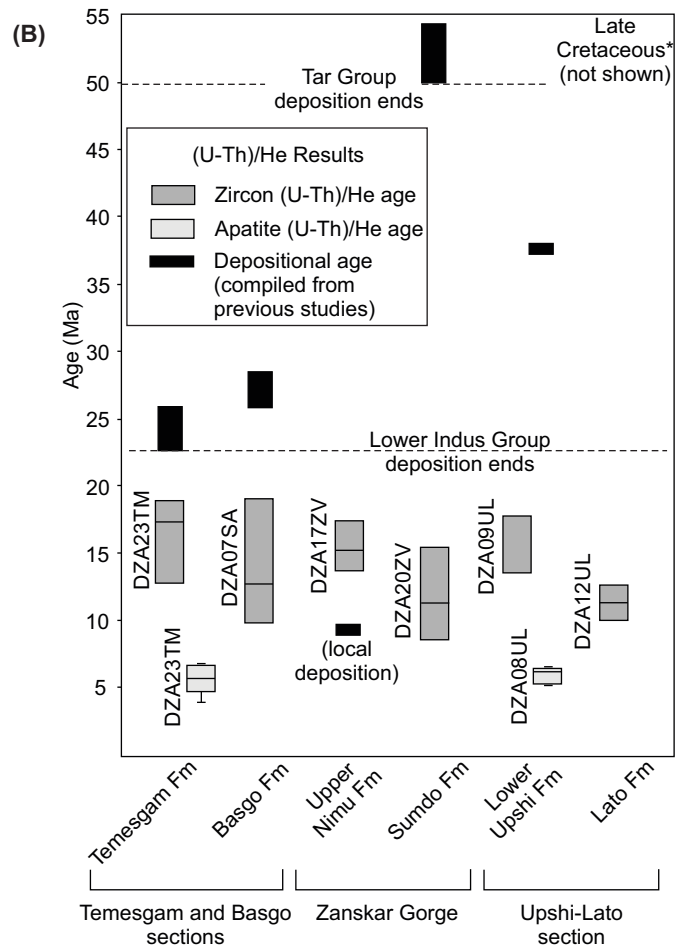
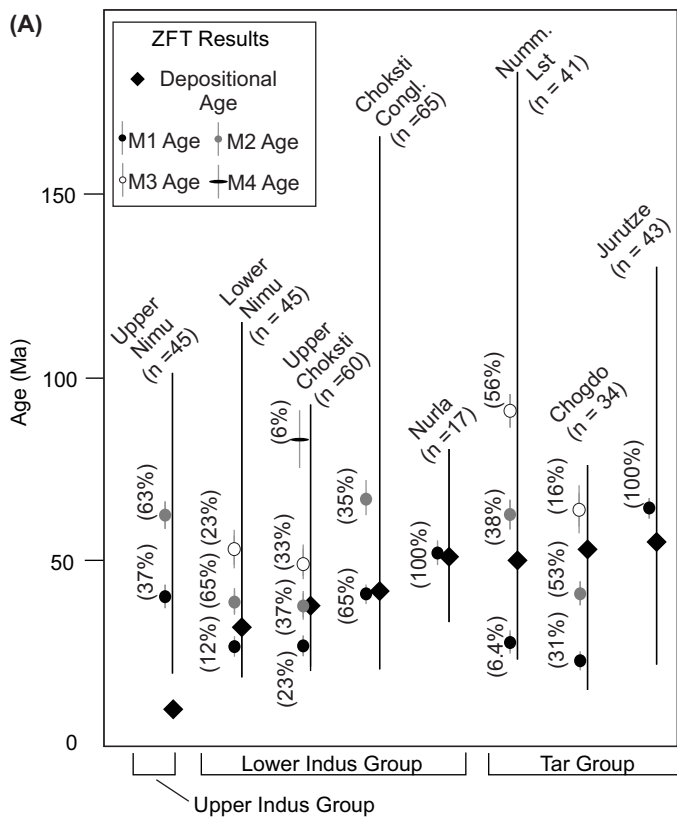


**Figure 3**



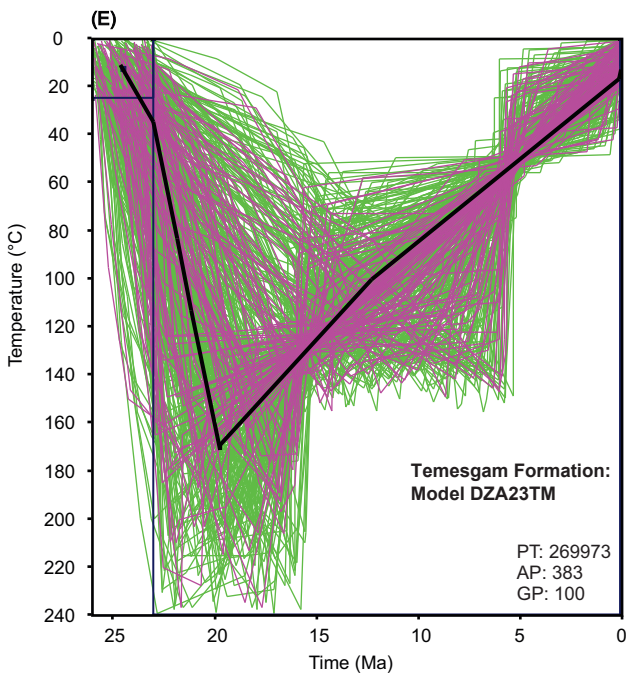
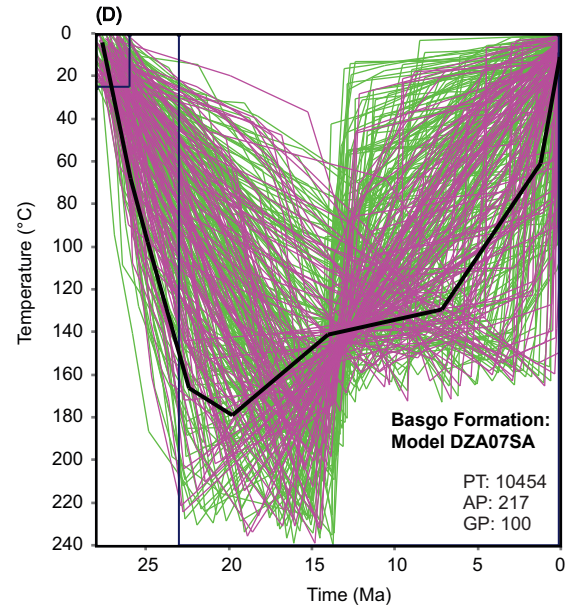
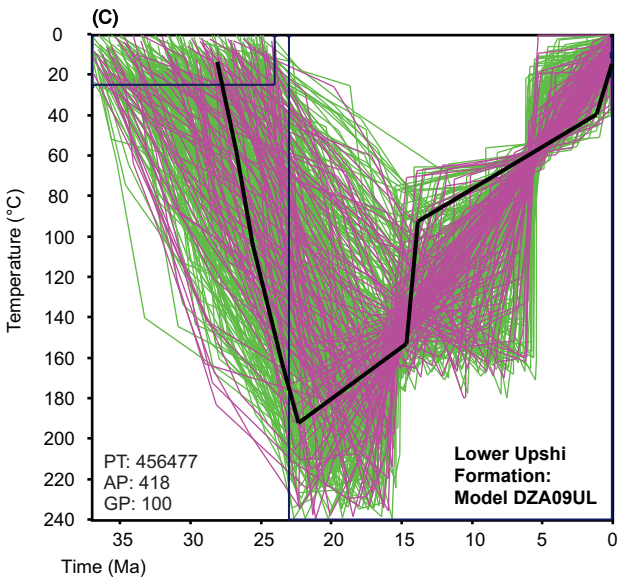
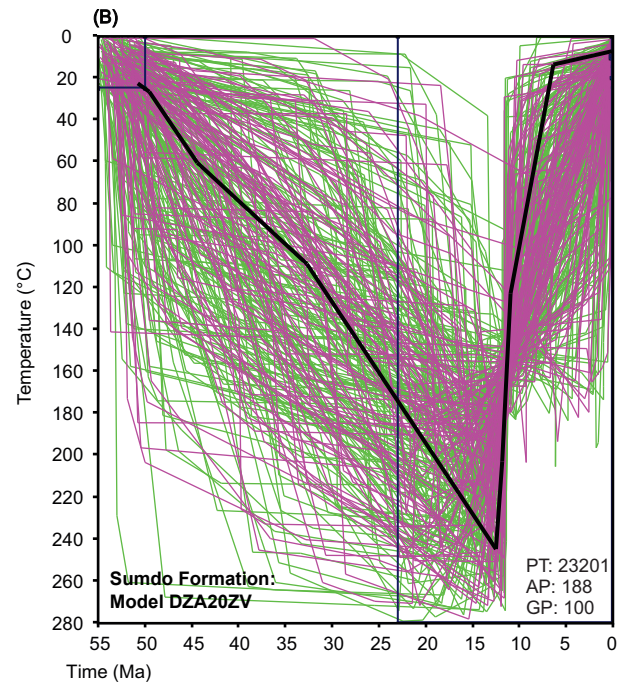
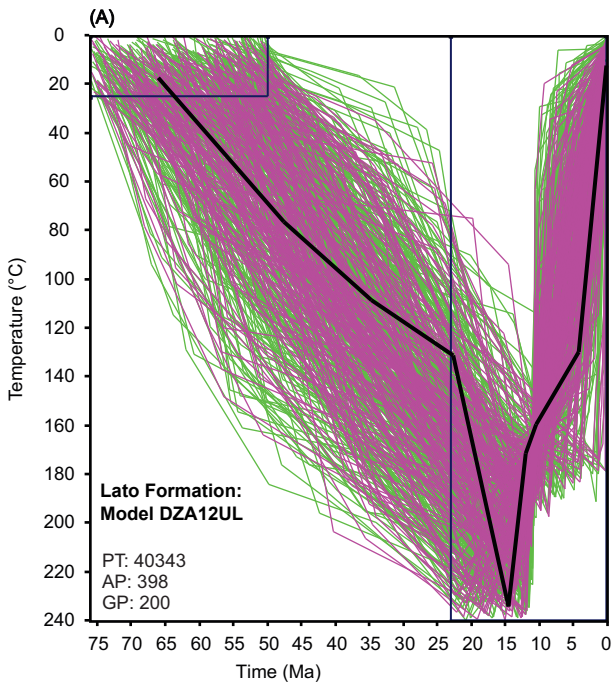


**Figure 4**

Table 1: Published stratigraphic schemes compared across the IBSR sections in NW India

Group (Age)		Temesgam and Basgo sections <sup>[1]</sup>	Zanskar Gorge <sup>[2]</sup>	Upshi-Lato section <sup>[3]</sup>		Composite Indus Group <sup>[4]</sup>	
				(north)	(south)		
Indus Group (Early Eocene – Pliocene)	Upper Indus Group (Pliocene)		Upper Nimu Formation (f) [9.5 ± 0.5 Ma]**			Local Pliocene strata (f)	
	Lower Indus Group (Early Eocene – Early Miocene)	Temesgam Formation	Basgo Formation [~28 Ma] <sup>#</sup>	Lower Nimu Formation (f) [32.3 ± 0.2 Ma]**	Upper Upshi Formation [24.6 ± 0.1 Ma]**	Rong Formation [50.0 ± 0.2 Ma]**	Temesgam Formation [26.8 ± 0.1 Ma]* Basgo Formation (f)
		(inaccessible)			Lower Upshi Formation (f) [38.3 ± 0.2 Ma]**		Nimu Formation Hemis Formation (f) [37.8 ± 0.2 Ma]*
		Choksti Formation	Upper Choksti Member	Upper Umlung Formation	Choksti Formation (f)		
			Middle Choksti Member	Lower Umlung Formation (f)			
			Red Shale Member (f)	Artsa Formation			
	Choksti Conglomerate (f)	Gonmaru La Formation (f)					
Nurla Formation (inaccessible)	Nurla Formation [51.8 ± 0.2 Ma]*	Stratigraphy absent	Nurla Formation (f) [50.7 ± 0.3 Ma]*				
Tar Group (Late Cretaceous – Early Eocene)			Nummulitic Limestone [~50 Ma] <sup>#</sup>	Miru Formation (f) [54.9 ± 0.2 Ma]*		Marine strata	
			Chogdo Formation [52.1 ± 0.1 Ma]*				
			Sumdo Formation [~55-51 Ma] <sup>#</sup>				
			Jurutze Formation (f) [54.7 ± 0.3 Ma]*				
Indian margin (Cretaceous)			Chilling Formation	Lato Formation			

Note: [1] Garzanti and Van Haver (1988), Bajpai et al. (2004), Tripathy-Lang et al. (2013), [2] Wu et al. (2007), Henderson et al. (2010), [3] Henderson et al. (2011), [4] Bhattacharya et al. Symbols: \* - U-Pb detrital zircon maximum depositional age, \*\* - 40Ar/39Ar detrital muscovite maximum depositional age, # - biostratigraphic age, f - the formation or member has a fault with the unit immediately below or older; bold dashed line indicates unconformity. Maximum depositional ages are YC2σ(3+) ages, which is the weighted average of youngest 3 or more grain ages with overlapping 2σ uncertainties. All uncertainties are reported at 1σ uncertainty level.

Table 2: Summary of ZFT, ZHe and AHe ages from Zaskar Gorge, Upshi-Lato, Basgo and Temesgam sections

Section	Group	Formation	Member	Maximum Depositional Ages (Ma)			Fossil Age (Ma)	Thermochronometric Ages (Ma)			Interpretation
				YSG	YC1 $\sigma$ (2+)	YC2 $\sigma$ (3+)		ZHe Range	AHe Range		
Zaskar Gorge	upper Indus	Upper Nimu		DM: 6.1 $\pm$ 2.3	6.7 $\pm$ 1.5	<b>9.5 <math>\pm</math> 0.5</b>		M1: 40.2 $\pm$ 3.1 M2: 62.7 $\pm$ 3.5 (ZG16)	17.39 $\pm$ 0.35 - 13.70 $\pm$ 0.27 (DZA17ZV)		Unreset w.r.t ZFT and ZHe
	lower Indus	Lower Nimu		DM: 23.7 $\pm$ 0.2	32.3 $\pm$ 0.2	<b>32.3 <math>\pm</math> 0.2</b>		M1: 25.5 $\pm$ 3.1 M2: 38.5 $\pm$ 2.7 M3: 53.8 $\pm$ 5.8 (ZG21)			Partially reset w.r.t ZFT
			Upper Choksti*	DZ: 36.8 $\pm$ 0.6 (H) DM: 37.6 $\pm$ 0.4 (LU)	37.3 $\pm$ 0.3 (H) 38.9 $\pm$ 0.2 (LU)	<b>37.8 <math>\pm</math> 0.2 (H)</b> <b>38.3 <math>\pm</math> 0.2 (LU)</b>		M1: 26.6 $\pm$ 2.2 M2: 37.8 $\pm$ 3.8 M3: 49.5 $\pm$ 4.4 M4: 83 $\pm$ 8.4 (ZG30)			Partially reset w.r.t ZFT
			Choksti								
			Choksti Conglomerate	DZ: 41.1 $\pm$ 0.3	42.0 $\pm$ 0.4	<b>41.5 <math>\pm</math> 0.2</b>		M1: 40.3 $\pm$ 2.1 M2: 68.6 $\pm$ 4.1 (ZG38)			Partially reset w.r.t ZFT (see text for explanation)
			Nurla	DZ: 51.0 $\pm$ 0.5 DZ: 49.5 $\pm$ 0.7 (EL)**	51.5 $\pm$ 0.2 50.2 $\pm$ 0.4 (EL)	<b>51.8 <math>\pm</math> 0.2</b> <b>50.7 <math>\pm</math> 0.3 (EL)</b>		M1: 50.3 $\pm$ 3.3 (ZG42)			Partially reset w.r.t ZFT
		Tar	Nummultic Limestone	DZ: 52.5 $\pm$ 0.4	89.6 $\pm$ 0.3	90.2 $\pm$ 0.2	<b>-50</b>	M1: 27.8 $\pm$ 3.5 M2: 62.6 $\pm$ 4.4 M3: 91.1 $\pm$ 5.5 (ZG62)			Partially reset w.r.t ZFT (see text for explanation)
			Chogdo	DZ: 50.8 $\pm$ 0.5	51.3 $\pm$ 0.3	<b>52.1 <math>\pm</math> 0.1</b>		M1: 22.5 $\pm$ 2 M2: 40.3 $\pm$ 3 M3: 63.8 $\pm$ 6.4 (ZG55)			Partially reset w.r.t ZFT
			Sumdo				<b>-55-51</b>		15.42 $\pm$ 0.20 - 8.57 $\pm$ 0.11 (DZA20ZV)		Reset w.r.t ZHe
			Jurutze	DZ: 53.4 $\pm$ 0.7	53.7 $\pm$ 0.5	<b>54.7 <math>\pm</math> 0.3</b>		M1: 65.2 $\pm$ 3.1 (ZG45)			Partially reset w.r.t ZFT (see text for explanation)
Upshi-Lato	lower Indus	Upper Upshi		DM: 24.4 $\pm$ 0.2	24.4 $\pm$ 0.2	<b>24.6 <math>\pm</math> 0.1</b>					
		Lower Upshi		DM: 37.6 $\pm$ 0.4	38.9 $\pm$ 0.2	<b>38.3 <math>\pm</math> 0.2</b>			17.79 $\pm$ 0.26 - 13.63 $\pm$ 0.21 (DZA09UL)	6.56 $\pm$ 0.10 - 5.22 $\pm$ 0.30 (DZA08UL)	Reset w.r.t ZHe and AHe
		Umlung/Artsa/ Gonmaru La									
		Tar	Miru	DZ: 54.3 $\pm$ 0.4	54.7 $\pm$ 0.2	<b>54.9 <math>\pm</math> 0.2</b>					
	Indian margin unit	Lato	DZ: 51.1 $\pm$ 0.4 DM: 67.2 $\pm$ 1.13 DZ***: 159.2 $\pm$ 2.0 (CF)	481.0 $\pm$ 2.5 375.8 $\pm$ 1.0 451.6 $\pm$ 3.9 (CF)	484.3 $\pm$ 1.7 376.3 $\pm$ 1.0 456.4 $\pm$ 3.4 (CF)			12.62 $\pm$ 0.26 - 10.05 $\pm$ 0.20 (DZA12UL)		Reset w.r.t ZHe	
Basgo and Temesgam	lower Indus	Temesgam		DZ: 26.2 $\pm$ 0.5	26.7 $\pm$ 0.1	<b>26.8 <math>\pm</math> 0.1</b>			18.91 $\pm$ 0.52 - 12.81 $\pm$ 0.18 (DZA23TM)	6.77 $\pm$ 0.40 - 3.94 $\pm$ 0.17 (DZA23TM)	Reset w.r.t ZHe and AHe
		Basgo		DZ: 27.2 $\pm$ 0.5	52.6 $\pm$ 0.2	53.4 $\pm$ 0.1	<b>-28-26</b>		19.04 $\pm$ 0.54 - 9.90 $\pm$ 0.27 (DZA07SA)		Reset w.r.t ZHe

Note: Maximum depositional ages and fossil ages are compiled from Bajpai (2004), Green et al. (2008), Wu et al. (2007), Henderson et al. (2010, 2011), and Bhattacharya et al. (2020). Youngest cluster ages, i.e., YC1 $\sigma$ (2+) and YC2 $\sigma$ (3+), if unreported in previous studies, were recalculated using detritalPy (Shaman et al., 2018). Details about the methods of maximum depositional age recalculation can be found in Dickinson and Gehrels, (2009). For thermochronometric interpretations, if fossil ages (bold) are unavailable for a formation, we consider the corresponding YC2 $\sigma$ (3+) age (bold), which is the most conservative estimate of maximum depositional age (Coutts et al., 2019). Abbreviations: YSG - youngest single grain, YC1 $\sigma$ (2+) - weighted mean age of youngest cluster of at least 2 ages with overlapping 1 $\sigma$  uncertainties, YC2 $\sigma$ (3+) - weighted mean age of youngest cluster of at least 3 ages with overlapping 2 $\sigma$  uncertainties, DZ - detrital zircon maximum depositional age, DM - detrital muscovite maximum depositional age, w.r.t - with respect to. \*Upper Choksti Member is correlatable with the Hemis (H) and Lower Upshi (LU) Formations, and the corresponding maximum depositional ages are provided (Henderson et al., 2011; Bhattacharya et al., 2020). \*\* (EL) indicates the maximum depositional ages of the Nurla Formation from eastern Ladakh. \*\*\*Lato Formation is also correlatable to the Indian plate Chilling Formation (CF) whose maximum depositional ages are provided (Henderson et al., 2011).

Table 2. Summary of ZFT, ZHe and AHe ages from Zaskar Gorge, Upshi-Lato, Basgo and Temesgam sections. Depositional ages were compiled from stratigraphic works of Bajpai et al. (2004), Green et al. (2008), Wu et al. (2007), Henderson et al. (2010, 2011), Bhattacharya et al. (2020).